Universidade do Minho
Escola de Engenharia

Marisa Alexandra Pinheiro Silva

Development of microstructures for application on a controllable bioinspired adhesive mechanism for gripping system in pick-n-place task

outubro de 2022

Development of microstructures for application on a controllable bioinspired adhesive mechanism for gripping system in pick-n-place task

Marisa Silva

UMINHO| 2022

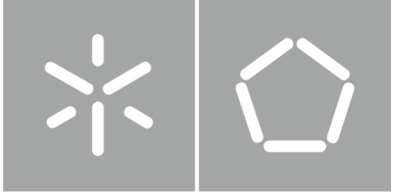

Universidade do Minho
Escola de Engenharia

Marisa Alexandra Pinheiro Silva

Development of microstructures for application on a controllable bioinspired adhesive mechanism for gripping system in pick-n-place task

Dissertação de Mestrado
Mestrado Integrado em Engenharia Mecânica

Trabalho efetuado sob a orientação do Professor:
Rui Alberto Madeira Macedo de Lima
E coorientação do Doutor:
Aritz Retolaza

outubro de 2022

DIREITOS DE AUTOR E CONDIÇÕES DE UTILIZAÇÃO DO TRABALHO POR TERCEIROS

Este é um trabalho académico que pode ser utilizado por terceiros desde que respeitadas as regras e boas práticas internacionalmente aceites, no que concerne aos direitos de autor e direitos conexos.

Assim, o presente trabalho pode ser utilizado nos termos previstos na licença abaixo indicada.

Caso o utilizador necessite de permissão para poder fazer um uso do trabalho em condições não previstas no licenciamento indicado, deverá contactar o autor, através do RepositóriUM da Universidade do Minho.

AGRADECIMENTOS

Há numerosas contribuições que devem ser destacadas na conclusão desta dissertação. Gostaria de agradecer sinceramente a todas as pessoas e entidades que contribuíram significativamente para o desenvolvimento deste trabalho.

Antes de mais, ao Professor Rui Alberto Lima, um dos orientadores do projeto, pela sua orientação e pelo tempo que disponibilizou para reuniões, esclarecimento de dúvidas, e elucidação dos vários tópicos abordados.

Um grande agradecimento também ao Doutor em Química Aritz Retolaza, orientador na empresa, e ao Engenheiro Edoardo Sotgiu pela ajuda infinita ao longo de todo o projeto e por todos os meses disponibilizados para a orientação do mesmo. A todos os colaboradores da INL, pela simpatia com que fui recebida e pela transmissão de todos os conhecimentos necessários.

Ao INL, por permitir que a dissertação fosse concluída nas suas instalações e por oferecer as ferramentas e condições necessárias para o seu desenvolvimento.

Finalmente, à minha família. Aos meus pais e à minha irmã, pela oportunidade de fazer este curso académico, por todos os valores transmitidos e pelos numerosos momentos compartilhados de felicidade.

STATEMENT OF INTEGRITY

Declaro ter atuado com integridade na elaboração do presente trabalho académico e confirmo que não recorri à prática de plágio nem a qualquer forma de utilização indevida ou falsificação de informações ou resultados em nenhuma das etapas conducente à sua elaboração.

Mais declaro que conheço e que respeitei o Código de Conduta Ética da Universidade do Minho.

Universidade do Minho, 31 de outubro de 2022

RESUMO

A natureza oferece uma variedade de ideias para uma adesão transitória e reversível a diferentes substratos. Até agora, os *soft dry adhesives* (SDAs) bioinspirados mais estudados são superfícies com matrizes de micropilares. A inspiração veio de espécies terrestres, como as osgas, cujas almofadas dos pés são cobertas por intrincadas fibrilhas que permitem uma forte adesão (que se deve a forças intermoleculares) bem como uma fácil libertação.

Um dos objetivos atuais dos esforços da investigação é transferir a solução da natureza para estruturas artificiais que possam um dia encontrar aplicações tecnológicas. Este trabalho visa replicar os comportamentos de agarra e libertação das osgas, utilizando como base as suas estruturas fibrilares pegajosas. Para este objetivo, serão utilizadas várias técnicas de fabrico e ensaios experimentais para determinar o melhor protocolo para a criação de microestruturas. Foram estudados micropilares cilíndricos lisos e micropilares com forma de cogumelo, tendo sido escolhidos estes últimos dado que aderem melhor aos substratos lisos em comparação com pilares cilíndricos.

O presente trabalho começou por delinear o estado de arte, no qual se investiga o desenvolvimento de SDAs bioinspirados e as suas qualidades adesivas. Além disso, também foram abordados os fundamentos de adesão fibrilar. Prosseguiu-se para o desenvolvimento de amostras em polidimetilsiloxano (PDMS) com o objetivo de caracterizar este material num equipamento de ensaio universal (UTM).

Neste trabalho foram examinadas várias técnicas de microfabricação. Tendo em consideração a dimensão das micropartículas utilizadas, foram produzidas microestruturas utilizando uma metodologia de baixo custo. Foram utilizados e testados vários tipos de métodos para fabricar os moldes, ou seja, para produzir pilares cilíndricos lisos foi utilizada fresagem e para produzir micropilares em forma de cogumelo foi utilizada impressão 3D. Devido à sua forma, os micropilares em forma de cogumelo requerem uma dupla moldagem, com um molde intermediário constituído por um material altamente flexível.

Finalmente, com o auxílio do UTM para realizar testes de aderência, foi avaliada a eficiência das microestruturas.

Palavras-Chave

ADESÃO; BIOINSPIRAÇÃO; IMPRESSÃO 3D

ABSTRACT

Nature offers a variety of ideas for transient and reversible adhesion to different substrates. Geckos and insects use hairy structures whose adhesion is due to intermolecular forces. So far, the most widely studied SDAs are surfaces with arrays of micropillars. The inspiration came from terrestrial species including lizards and geckos whose toe pads are covered by intricate fibrils that enable strong attachment as well as easy release.

The current goal of research and development efforts is to transfer nature's solution into artificial structures that might someday be applied in different technologies. Hence, this work aims to replicate the grasping and releasing behaviors of geckos using their fibrillar sticky structures as a basis. In order to achieve this goal, different kinds of designs, fabrications, and testing will be used to determine the best protocol for creating microstructures. Smooth cylindrical and mushroom-shaped micropillars were studied. The latter were chosen because they adhere to smooth substrates better than cylindrical micropillars.

This work began by outlining the state of the art on the development of soft dry adhesives (SDAs) with natural inspiration and an examination of their dry adhesive properties. Additionally, the fundamentals of fibrillar adhesion were also covered. The work then proceeded to the development of polydimethylsiloxane (PDMS) specimens with the goal of characterizing this material in a universal testing machine (UTM).

A number of microfabrication techniques were examined. Based on the size of the employed microparticles, microstructures were produced applying a low-cost method. Different methods were employed depending on the shape of the molds, i. e., to produce cylindrical flat pillars, it was used a CNC milling machine whereas to produce mushroom shaped micropillars, it was used 3D printing. Due to their design, the micropillars with the mushroom shape required double molding with an intermediary mold made of a highly flexible material.

Finally, using the UTM to perform adhesion tests, the efficiency of the microstructure was evaluated.

Keywords

ADHESION; BIOINSPIRATION; 3D PRINTING

TABLE OF CONTENTS

INDEX OF FIGURES

INDEX OF TABLES

LIST OF SYMBOLS

Abbreviations and acronyms

MRES	Magnetorheological elastomers
PDMS	Polydimethylsiloxane
PFOTS	Trichloro(1H,1H,2H,2H-perfluorooctyl)silane
SDA	Nature-inspired Soft Dry Adhesives
UTM	Universal Testing Machine.

Nomenclature

P_c	pull-off force (mN)
E	Young's modulus (MPa)
E*	reduced Young's modulus (MPa)
σ_c	pull-off strength (kPa)
R	pillar radius (µm)
s	interpillar spacing (µm)
w	work of adhesion (J/m^2)
AR	pillar aspect ratio (−)
v	Poisson's ratio (−)
G	Energy release rate (J),

1. INTRODUCTION

Nature provides many concepts for temporary and reversible adhesion to various substrates, e.g. on plants and animals. Geckos and insects use hairy structures whose adhesion is due to intermolecular forces (Autumn et al., 2002).

Transferring nature's solution into artificial structures that may eventually find technological applications is the current objective of research and development efforts. Many reversible attachment systems (Paretkar et al., 2011) based on micropatterns have been investigated in the literature (Balijepalli et al., 2017).

There are artificial adhesives that have a high adhesion strength however they can be difficult to detach. Additionally, they are difficult to reuse due to how easily adhering materials contaminate the surfaces as a result of their sticky nature.

Engineered soft adhesives (binding agents between two surfaces that are flexible and conformable are called soft adhesives) are now a common occurrence in our daily lives, such as double-sided tape for paper sticking, flexible brace tapes for protecting joints, and medical bandages for treating wounds. Typically, soft adhesives fall into one of two categories: soft wet adhesives (SWAs) or soft dry adhesives (SDAs) (Figure 1.1). SWAs bind surfaces collectively by means of mechanical stress or chemical processes. Pressure-sensitive adhesives (PSAs), for instance, are a well-known type of SWAs that contain a viscoelastic bonding ingredient that may instantly attach to the adherend when pressure is applied (L. Wang et al., 2020).

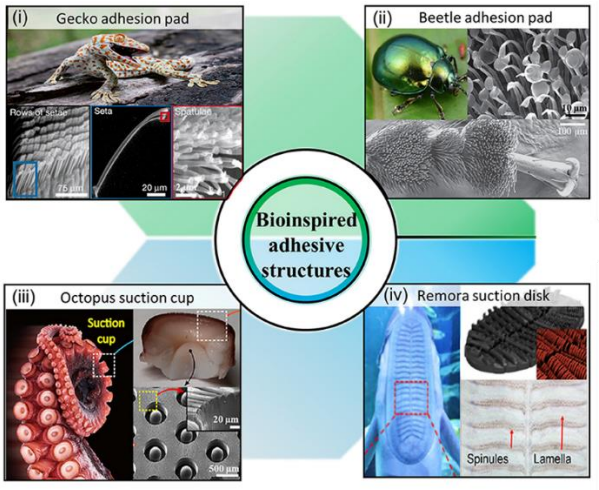

Figure 1.1 – Schematics of bioinspired adhesive structures for reversible dry and wet adhesion. Representative examples of adhesive structures in nature: (i) gecko's toes; (ii) beetle's pads (iii); octopus suction; (iv) remora suction disk (Kang et al., 2021).

PSAs, like adhesive tapes, are made of sticky, viscoelastic polymers that are soft and pliable. These materials experience extensive plastic deformation during debonding as well as spontaneous plastic deformation that increases the true area of contact with the surface at the nanoscale (Autumn, 2007).

It is of note that objects are never perfectly flat due to asperities. Therefore, because only a fraction of the nominal area made up of one object's atoms is in true contact with the atoms of the other object when two objects contact, the true area of contact (on a microscopic scale) is usually only a fraction of the apparent contact area on a macroscopic scale.

Gecko setae (microscopic foot hairs) arrays have low bending stiffness and are relatively conformable to the substrate. As such, because they lack 3D connections, they might resist stress concentration because the contact areas may be independent and evenly distribute the load. In fact, theoretical considerations suggest that the gecko adhesive's fibrillar structure, as opposed to a solid layer of sticky material, may enhance the debonding energy by reducing the stress concentrations required for a fracture to spread. Additionally, setae structures, in contrast to polymer phenomenon, could release energy largely through elastic rather than plastic mechanisms (Autumn, 2007). Each seta of the array may retain debonding stress elastically and as the setae are removed, elastic energy may be lost internally without assisting crack propagation (Autumn, 2007).

Dry adhesion is controlled by physical rather than chemical interactions. Van der Waals and electrostatic forces, friction, and suction are a few examples of physical interactions. Although, dry attachment systems (e.g., in spiders and geckos) are believed to rely almost entirely on intermolecular van der Waals forces between the finely structured spatulae and the substrate, and, to some extent, to capillary forces.

Gecko lizards' dry adhesion process has drawn a lot of interest since it enables powerful, yet reversible attachment to surfaces with various degrees of roughness and orientation. Millions of setae, which divide into hundreds of smaller, nanoscale endings (spatulae), are responsible for the remarkable capacity of surfaces to adhere to one another by van der Waals forces.

Such a hierarchically organized structure (Figure 1.2) results in a soft and compliant surface, which allows easy adaption to roughness at the expense of little strain energy and thus enhances adhesion (Hensel et al., 2018).

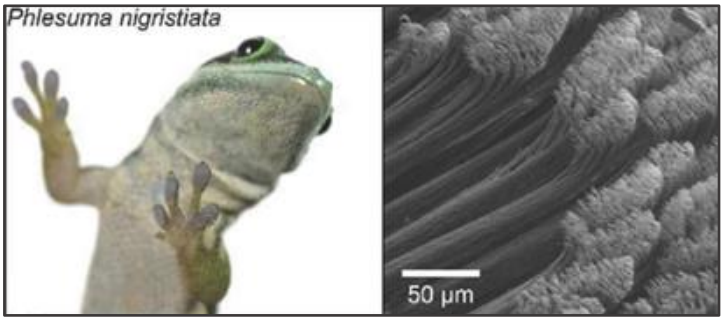

Figure 1.2 – The hierarchical adhesive structure of a gecko toe (left) containing hundreds of thousands of setae. Scanning electron image showing setae splitting into finer spatular structures (right) (Hensel et al., 2018).

Reversible or switchable adhesives are of particular fascination for research groups. Reversibility enables repeated cycles of attachment and detachment without damaging the contact between the adhering objects or the objects themselves (Hensel et al., 2018). There is developing evidence that what may enable the gecko adhesive to tolerate repeated use without creep or degradation is the occurrence that an array of gecko setae can act like a deformable material, while individual setae and spatulae retain the structural integrity of stiff protein fibbers (Autumn, 2007).

With the rapid development of bioelectronics and the increasing demand for seamless integration between humans and machines, conventional SWAs are facing some challenges. Despite their relatively strong bonding capability, the binding agent can be easily contaminated with impurities (e.g., dust, sebum, etc.), limiting both the ability to reposition and reuse.

1.1. Objectives and Motivation

Numerous studies over the past decades have shown that biomimetics is a very effective strategy to develop surfaces with novel functional characteristics, such as self-cleaning, drag reduction, and physical colour patterns. Additionally, biological attachment mechanisms are a valuable source of knowledge for the development of novel adhesives. Geckos, in particular, have been the subject of many studies on attachment development.

Gecko feet do not adhere to surfaces like tape does. The lizards instead rely on millions of microscopic hair-like protrusions that, when bent due to a phenomenon called van der Waals forces, become extremely adhesive.

The main expected results of this work are the development and optimization of microstructures for application on a controllable bioinspired adhesive mechanism for gripping system in pick-n-place task.

The aim of the work is to emulate geckoes' gripping and releasing methods, which depend on their fibrillar adhesive structures.

The work can be divided into the following objectives:

- Investigate the fabrication technologies.
- Characterization of the PDMS material properties.
- Investigate and optimize the fabrication processes.
- Optimize the microstructures geometry.
- Evaluation of the device efficiency.

Towards this effort a cyclic process of design, fabrication, and test (optical inspection) is conducted in order to reach the definition of the optimal recipes for the fabrication process of microstructures with shapes such as mushroom tip. For that, fabrication processes such as 3D printing and CNC milling will be used.

1.2. INL PRESENTATION

The INL International Iberian Nanotechnology Laboratory, located in Braga (North of Portugal) was founded by the governments of Portugal and Spain under an international legal framework to perform interdisciplinary research, deploy and articulate nanotechnology for the benefit of society. The Research and Technology activities are focused on six clusters: Health, Food, Energy, Environment, ICT (Information and Communication Technologies) and Future Emerging Technologies, which complement each other and provide a base for interdisciplinary interactions.

The present work was developed in the Integrated Micro and Nanotechnologies (IMiNa) research group at INL. The research activity of the Integrated Micro and Nanotechnologies group (IMiNa) is focused on developing and exploring new micro and nanotechnologies and developing devices to tackle high-impact challenges and address industry, market, and scientific trends. The group presents a broad scientific background in materials, physics, electronics, mechanics, optics, chemistry, engineering and microfluidics. Focusing on micro and nanotechnology, the competencies in sensors and device development range from

modelling, design, and fabrication (extensive experience in state-of-the-art microfabrication techniques and tools), characterization (including electronic design, instrumentation and data analysis), integration and packaging.

2. LITERATURE REVIEW

Adhesion is a fundamental phenomenon that plays a significant role in technology, everyday life, and nature. Nearly all kinds of matter display adhesion, or the mutual attraction of things in contact, as a universal phenomenon. Solutions for regulating adhesion have developed throughout the history of biological evolution, allowing organisms to cling to solids either temporarily or permanently in a variety of situations. For typical ambient conditions, for high and low temperatures, for fluctuating humidity, and even for submerged situations, such natural solutions exist (Hensel et al., 2018). To produce new mechanical devices, these ideas are currently being translated into technical solutions, particularly in the automation and robotics fields.

2.1. BIOINSPIRED SOFT DRY ADHESIVES (SDAS)

So far, the most widely studied SDAs are surfaces with arrays of micropillars. The inspiration came from terrestrial species like the gecko, whose toe pads are covered by intricate fibrils that enable strong attachment as well as easy release.

The fibrillar foot pad organs of insects, spiders, and lizards are the most fascinating examples of reusable adhesives found in nature. They are designed to move over different kinds of surfaces by attaching and detaching in milliseconds. For evolutionary biologists, the fact that many foot pads have elongated fibrillar structures with aspect ratios varying from 10 to 80 and terminal parts provides a variety of contact shapes, ranging from spherical to conical, filament-like, toroidal, and concave terminals is important (Hensel et al., 2018).

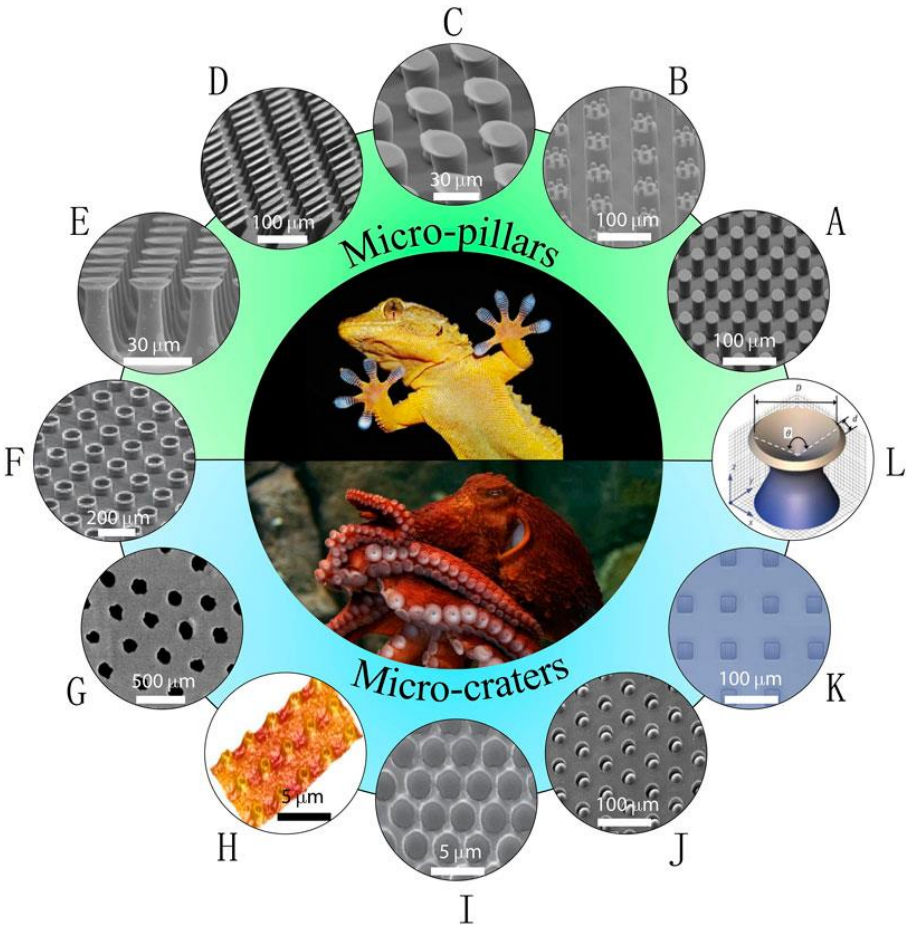

Figure 2.1 – Examples of nature-inspired soft dry adhesives (SDAs). (A–E) Gecko-inspired synthetic micropillars with various tip geometries: (A) flat tip; (B) hierarchical tip; (C) spatular tip; (D) slanted tip; (E) mushroom-like tip. (F) A combinational structure – micropillars with concave tip. (G–K) Octopus-inspired synthetic micro-suckers or craters: (G) nano-craters on UV resin surfaces; (H) reversible adhesive skin patch with micro-craters on multilayer PDMS; (I) micro-craters on PDMS surface; (J) micro-craters with interior protuberances; (K) square-patterned micro-craters on PDMS surface. (L) Combinational structure – pillar with funnel-shaped tip(L. Wang et al., 2020).

The Figure 2.1 showcases several synthetic micro-scale surface features resembling gecko fibrils. The simplest design being the micropillars with flat tips (del Campo & Arzt, 2007) (Figure 2.1 (A)). More advanced designs involve micropillars with hierarchy ((Greiner, Arzt, et al., 2009)) (Figure 2.1 (B)). Spatula tips (del Campo & Arzt, 2007; Del Campo et al., 2007) (Figure 2.1 (C)), which have been designed to mimic the gecko's toe pads more closely. Emulating the design principle of the tilting setae on gecko's toe pads, slanted structures have been widely exploited to generate directional adhesion (Figure 2.1 (D)) ((Moon et al., 2010; Murphy et al., 2008; Z. Wang, 2018)). This represents a breakthrough in developing reversible adhesives that truly resemble their natural prototypes. Among all the tip geometries, the mushroom-like shape (Figure 2.1 (E)) stands out as it exhibits large adhesive strength by reducing the stress concentration at the pillar-substrate interfaces (Del Campo et al., 2007; T.

Kim et al., 2016). Figure 2.1 (F–L) display examples of another type of SDAs, suction, or crater-based adhesives (L. Wang et al., 2020).

The primary properties of the ideal synthetic dry adhesive that mimics the properties of a real gecko foot are (Sameoto & Menon, 2010):

- Adhesion through van der Waals interactions.
- Anisotropic adhesion.
- A high pull-off to preload ratio.
- Low detachment force when required.
- Self-cleaning.
- Anti-self-matting/self-adhesion.
- A low to no adhesion state in the absence of shear.

Bio-inspired, artificial adhesive surfaces often feature surfaces with micropatterns made up of a collection of small, cylindrical pillars made, generally, of PDMS, PDMS compound material (He et al., 2014), polyurethane (Jeong et al., 2009), carbon-tube (Qu et al., 2008), or additional soft materials. These pillars can have diameters between sub-micron and sub-millimeters, and their length-to-diameter aspect ratios range typically within 1 and 10 (Table 2.1).

Table 2.1 – Review of several micropattern dimensions in literature (L. Wang et al., 2020).

Material	Modulus (MPa)	Normal adhesion (kPa)	Tip diameter min (µm)	Pillar length min (µm)	AR	Tip shape
Sylgard 184	1-10	111-219	40	100,00	1,25	Mushroom
Sylgard 184	1-10	100-180	10	20,00	1,00	Mushroom
Sylgard 184	0,76	5	10	30,00	1,50	Mushroom
PDMS	2-3	22,5	20	55,00	1,38	Mushroom
PDMS	2	13	5	5	1,25	Mushroom
PDMS	1,5-3,5	13	5	30,00	3,00	Mushroom
PDMS	2-3	12,5	13	80,00	3,08	Tilted
PDMS	2-3	10,5	-	100,00	-	Wedge
PDMS	2,8-8,2	7,5-18	5	20,00	2,00	Mushroom
PDMS	2-3	7,5-14	60	120,00	0,77	Mushroom

These pillars have been fabricated with a variety of tip shapes (flat-bottomed (Greiner et al., 2007) or mushroom-shaped (Gorb et al., 2007; Greiner et al., 2007)) and geometries. Such adhesive pillars have also been made from shape memory polymers and from flexible

nickel paddles coated with polymeric nanorods. A switchable adhesion has been achieved in such systems by controlling temperature, magnetic field, or compressive preload (Khaderi et al., 2015).

In the plot of Figure 2.2 the adhesion performance of structured surfaces with 3D pillars of different geometries was tested.

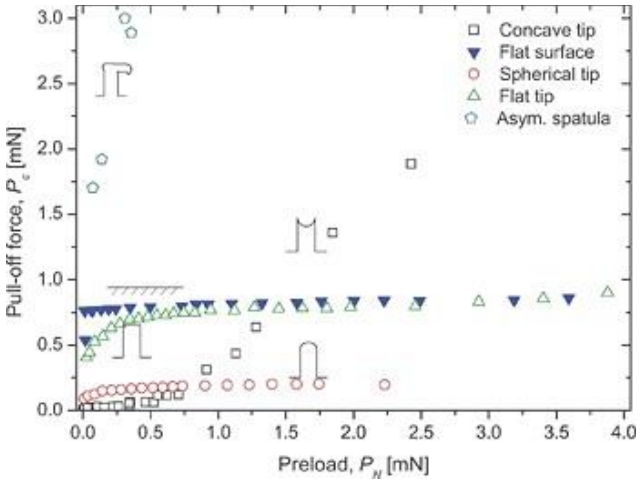

Figure 2.2 – Adhesion measurements obtained on structured Sylgard 184 surfaces with pillars of 10 µm in height, 10 µm in radius, and with different tip geometries. The plot shows the pull-off force, Pc, as a function of compressive preload. The experimental error corresponds to the size of the symbols (del Campo et al., 2007).

The flat tips result in the highest values for the optimum apparent contact strength. However, the required values for the optimal Young's moduli (approximately, 6 TPa) surpass moduli reached by the strongest materials (1 TPa). The value for the pillar aspect ratio is, also, very high (around 730), far above those reached by current nano- and micro-lithography techniques. On the other hand, carbon nanotubes exhibit aspect ratios of over 1000 and have, in recent experiments, demonstrated surprising adhesion capabilities (Greiner, Spolenak, et al., 2009).

When introducing surface roughness, the performance of the punch drops considerably, and the apparent contact strength gets about five orders of magnitude smaller than without roughness. Such drastic reductions in adhesion performance were modelled in the literature and have been found experimentally as well. For the other tip shapes, the spherical contact shows the second highest adhesion performance followed by the torus and the elastic tape (Greiner, Spolenak, et al., 2009).

Experimental research has shown that single-level structures made of long fibrils with seemingly flat ends frequently fail to meet of the theoretically projected increase in strength

considering contact area loss, lateral collapse, and fibril buckling. Enhancing adhesion is typically achieved in practice by developing an added terminal element at the end of a fibril (Aksak et al., 2011).

As it can be noted on the plot of the Figure 2.3, in del Campo et al. (2007) study on shape effects, the polydimethylsiloxane (PDMS) surfaces with mushroom-shaped fibrils were found to have a pull-off force that was roughly 20 times that of surfaces with fibrils with a simple cylindrical geometry, when they were pressed against a stiff, large diameter, spherical sapphire substrate and detached from it.

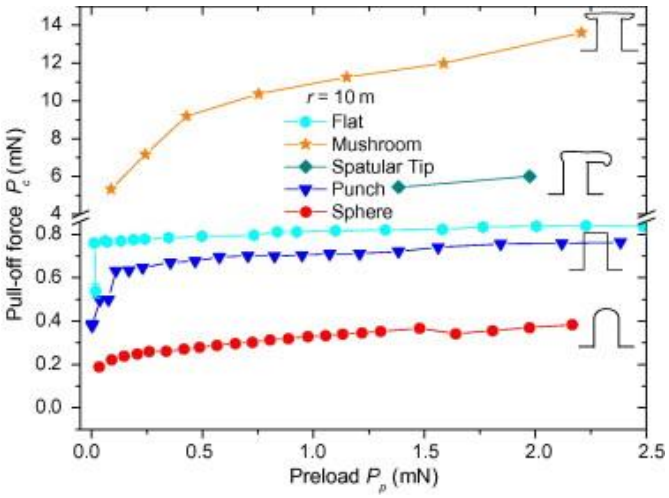

Figure 2.3 – Pull-off force vs. compressive preload for fibrils having various shapes but all with a shaft of 20µm diameter (Aksak et al., 2011; del Campo et al., 2007).

As mentioned before, according to experiments, compliant "mushroom" shaped fibrils achieve the highest adhesion. However, benefit from the mushroom cap is limited by three sources (Balijepalli et al., 2016) :

1. One source of the limitation is the inherent strength of the bond between the fibril and the substrate, which can lead to detachment commencing near the center of the fibril rather than at the edge.
2. Weak areas of bonding or of no bonding at all may be present near the center of the fibril, representing adhesion defects that may initiate detachment.
3. The strength of the fibril material itself may lead to the stalk of the fibril rupturing, since the mushroom shape leads to a stress in the stalk that is higher than the average stress at the interface with the substrate. This limiting factor is also corroborated by

the present study during the fabrication process there were a difficulty in not rupturing these fibrils during their fabrication.

2.2. MECHANICS OF FIBRILLAR ADHESION

The smallest level of hierarchical structure is patterned with finer fibrils; these data support the hypothesis that finer fibrils are related to improved adherence.

In the following subsections several parameters that affect the mechanics of fibrillar adhesion will be addressed.

2.2.1. CONTACT SPLITTING

The concept of contact splitting is one of the most interesting aspects of fibrillar adhesives. Adhesion between a fibrillar surface and a smooth substrate can be stronger than between two smooth surfaces. Furthermore, it is frequently noted that designs with small dimensions are superior to those with a coarser scale.

Fibrillar or patterned surfaces initially appear to be at a disadvantage since they produce a smaller area of adhesion with a substrate than a continuous, monolithic contact. However, this assessment makes the assumption that the adhesion force is proportionate to the contact area in light of more in-depth contact mechanics considerations. Due to a number of factors fibrillar components that interact with a substrate by short-range molecular effects (such as van der Waals forces) can show increased adhesion (Kamperman et al., 2010b).

The setae of animals studied are finely structured down to the µm and sub-µm levels. The diameters of their spatula-like terminal elements have been measured to range from 0,2 to 5,0 µm (Arzt et al., 2003). Comparative data, as it can be seen in Figure 2.4, shows clearly that the areal density of these terminal elements greatly increases with increasing body mass.

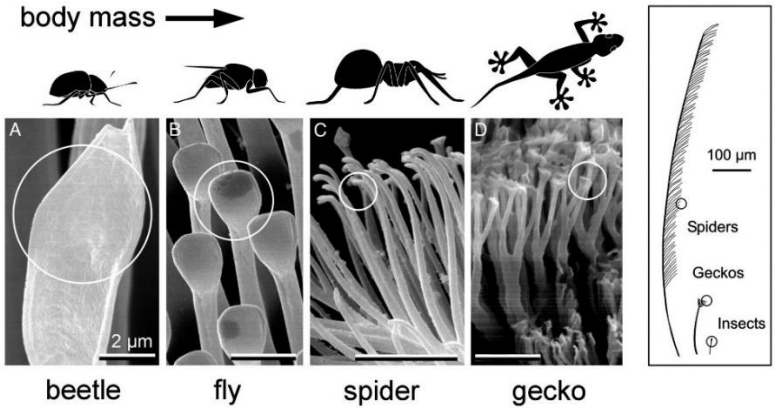

Figure 2.4 – Terminal elements in animals with hairy design of attachment pads. Note that heavier animals exhibit finer adhesion structures (Arzt et al., 2003).

The Johnson-Kendall-Roberts hypothesis of adhesion, developed initially for elastomeric materials, is based on the principle that small things always stick. This concept offered an explanation for adhesion increase by breaking one large contact into finer elements. Johnson-Kendall-Roberts highlights one of the fundamental principles of fibrillar adhesion despite its oversimplification: When an adhesive contact is created, elastic deformation enables surfaces to come together and allows the system to reduce surface area. In smaller contact elements, the “gain” in reduction of surface energy (a 2D effect) more easily offsets the elastic strain energy “penalty” (a 3D effect). This translates into higher adhesion strengths (Arzt et al., 2021).

The principle of contact splitting provided an explanation for the inverse correlation between attachment fibril diameter and animal mass: heavier animals exhibit finer contact elements, which hence “amplify” the effect of the van der Waals interaction.

Contact splitting effects can be categorized as (Kamperman et al., 2010b; Arzt et al., 2021; Autumn, 2006):

I. Contribution to the work of adhesion: Because the strain energy accumulated in a fibril shortly before pull-off is not accessible to induce detachment of the preceding fibril, fibrillar surfaces are more resistant to peeling. To put it another way, the detachment "crack" must be re-started fibril by fibril, with re-nucleation of peeling proving to be more challenging than its continuation.
II. Adaptability to rough surfaces: Long fibrillar components can adapt to the substrate's roughness with minimal strain energy loss. Hierarchical fibril structures exhibit this effect the most strongly.

III. Size effect due to surface-to-volume ratio: for small contacts, the penalty associated with the distortion required for accommodation, being controlled by volume, vanishes more rapidly than the surface energy gain. This favors the adhesion of smaller contact elements.

IV. Surface-to-volume effect: Fibrils show a more favorable balance between elastic strain and surface energy.

V. Uniform stress distribution in the contact: Below a critical diameter, fibrils are predicted to enter a defect-insensitive detachment regime and detrimental stress concentrations should disappear.

VI. Defect control and contact redundancy: The multiplicity of contacts reduces the sensitivity of the adhesive performance to local defects, delamination, and contamination. In other words, if adhesion defects control detachment, splitting up into finer contacts will limit defect sizes, and adhesion will be stronger. By contrast, a large defect in a monolithic contact is more damaging and will lead to easier detachment.

2.2.2. Aspect Ratio

A significant determinant for adhesion is the pillars' length-to-diameter aspect ratio. A large pillar height (and thus a large aspect ratio) is preferred for improving adhesion because a high aspect ratio results in a higher elastic energy wasted at pull-off (analogy to the mechanism of crack propagation in rubbery materials), which can yield a higher adhesion strength. However, it is necessary to take into consideration the preventing structural fracture (Y. Wang et al., 2014).

According to Greiner et al., 2007 the increase in the aspect ratio from 0,5 to 4 results in a 3-fold increase in Pc (at high preloads).

However, published data for the influence of the aspect ratio on the adhesion of patterned surfaces are contradictory. It was reported that the adhesion of poly-(vinyl butyral) fibrils, with E = 3.4 MPa, a radius of 1 mm, and aspect ratios between 1 and 15, has no influence of the increasing or decreasing aspect ratio (Glassmaker et al., 2005). It was also published a decrease in the adhesion force of pillar structures with a radius of 100 nm with an

increasing aspect ratio was also published (Lee et al., 2015), with measurements performed at aspect ratios of 1 and 3 (Greiner et al., 2007).

An important consequence related to the aspect ratio is the condensation (lateral collapse of pillars) that occurs when the adhesive forces between pillar tips in contact overcome the forces required for bending the pillar (Figure 2.5).

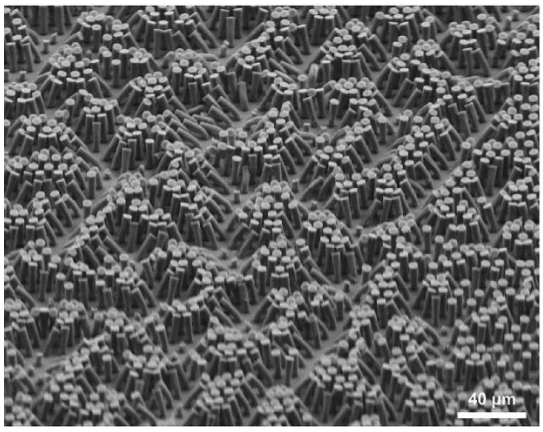

Figure 2.5 – SEM micrograph showing an array of pillars collapsed. This array was made by soft-molding Sylgard 184 onto SU-8 photolithographic templates (Greiner et al., 2007).

The condensation of pillars was observed in arrays with aspect ratios greater than 3, and the demolding step during fabrication seemed to be critical for avoiding condensation. Theoretical models predict critical aspect ratios for condensation between 2.5 and 5.2 for pillars (Greiner et al., 2007).

2.2.3. COLUMN BUCKLING

Column buckling is a phenomenon that happens when slender parts under extreme compression collapse; design measures can be taken to avoid this. The maximum load that a column can withstand prior to buckling can be determined by buckling load analysis. Elements including length, geometry stiffness, and material elasticity have an impact on this analysis. Instantaneity is another crucial aspect of the failure mode, which is precisely what makes it so dangerous and deceptive (Emil, 2021).

Elastic Buckling

Slender columns have higher risk of experiencing elastic buckling. This occurs at a level of stress that is less than the ultimate stress capacity of the material. It is due to instability in the column which results in failure.

The ideal column to resist buckling is the one that has homogenous cross-section and that it is initially straight. However, there are small imperfections in the structural elements related to fabrication and material.

It should be noted that buckling in columns can also be an effect of eccentric load. Which happens when the load line of action does not pass through the axis of the column, especially when the load line of action passes through a point considerably away from the axis of the column (Emil, 2021).

Buckling effect

Different end conditions relate to column buckling and the calculation of effective length. The effective length of the column (L_e) is equal to the effective length factor (K) times the length of the column (L). In Figure 2.6 each of the illustrations different end conditions of columns are demonstrated. The first scenario shows the end condition with one end fixed and another one free. The second scenario has both ends pinned. The third has one end fixed and the other end pinned. The fourth is presenting both ends fixed.

K represents the effective length factor which is dependent on the end condition of the column. Each of these illustrations helps in identifying the change in K (2, 1, 0.7 and 0.5) based on the end condition of the column. The length of the pinned-pinned column is the effective length of the column (L_e).

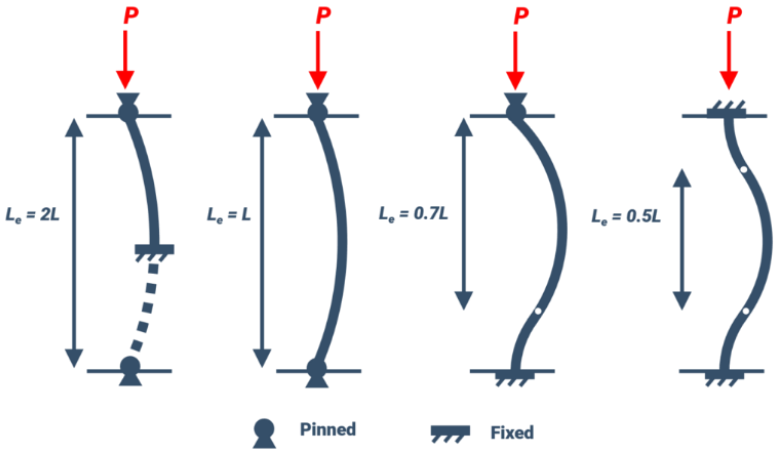

Figure 2.6 – Different end conditions related to column buckling and the calculation of effective length (L_e) can be identified by the illustration (Emil, 2021).

An important concept in the context is the critical load. It is the maximum compressive load in the axial direction which the column can resist before collapsing due to buckling. The formula given below can be used to calculate the critical load.

Generalization of Euler's formula for columns certain end conditions:

$$\sigma_{cr} = \frac{\pi^2 E.I}{KL^2}, \tag{2.1}$$

Where σ_{cr} , is the critical stress at which the column will buckle; E, Young's modulus of the material; I, Second moment of area of the cross section; K, The effective length factor; L, unsupported length of the column.

2.2.4. LIMITATIONS OF MICROPILLAR SDAS

Although there has been a substantial amount of research in the previous 20 years, there are still significant obstacles to micropillar-enabled SDAs in terms of applications. The adhesion can be improved by dividing the contact with the adherend into smaller subcontacts, which is made possible by incredibly small fibrils, according to the "contact splitting" notion (Arzt et al., 2003; Chan et al., 2007; Kamperman et al., 2010b)).

Scaling back the pillar size, however, faces important physical limitations and increases drastically the manufacturing challenges and costs. Both electron beam lithography (Vieu et al., 2000) and nanoembossing have acknowledged these difficulties (Becker & Heim, 2000; T. Kim et al., 2016, L. Wang et al., 2020).

Furthermore, slender pillars are prone to buckling and collapsing, resulting in undesirable entanglements and/or mats (see Figure 2.5). In fact, buckling may even lead to rupture and detachment (Chan et al., 2007; del Campo & Arzt, 2007; Greiner et al., 2007; D. S. Kim et al., 2007; T. Kim et al., 2016; L. Wang et al., 2020)

All of these degradation mechanisms have the potential to seriously reduce the adhesive's tensile strength, which would restrict its robustness and reusability. Aside from that, it has been extensively documented that in aquatic conditions or on wet surfaces, micropillars may lose their van der Waals adherence (L. Wang et al., 2020)

2.3. APPLICATIONS OF BIOINSPIRED SDAS

Dry adhesives are useful for a wide range of applications including climbing robots, pick-and-place handling of objects, Figure 2.7, and biomedical devices.

An example are the Gecko no-mark adhesive grippers launched by *OnRobot*. The technology requires no compressed air or external power, given that the pad uses millions of micro-scaled fibrillar stalks to adhere to a surface taking advantage of the van der Waals forces, saving costs and maintenance, and can be implemented on a robot arm for better production flexibility.

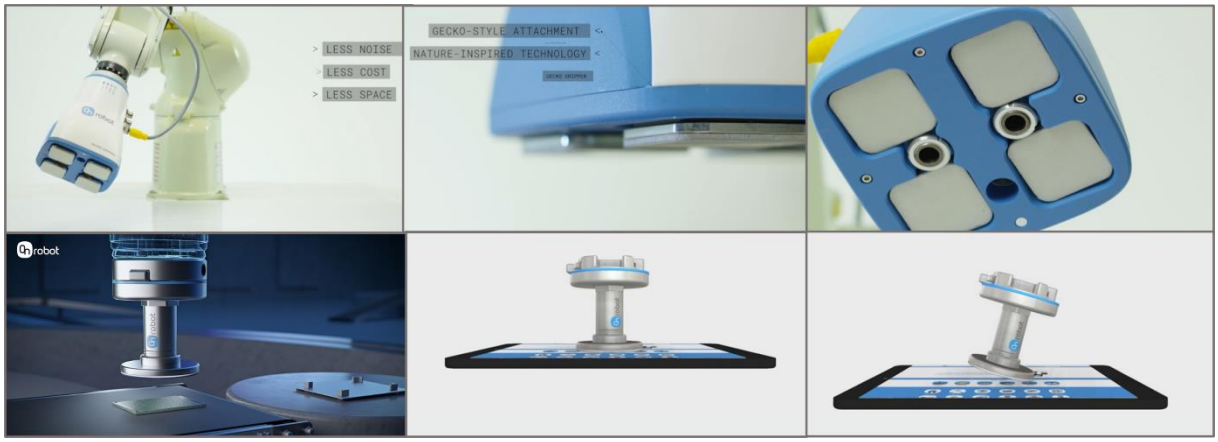

Figure 2.7 – Two examples of gripper solutions exploiting the gecko-like adhesion surface. The images on the right, demonstrate the release methods. The griper on the top image releases the surface by contracting its pads. The griper on the bottom as two ways of releasing: like it's exhibited in the picture, by tilting the gripper, or by clapping the piece in a fixture and moving the gripper (*OnRobot*, n.d.).

The gecko adhesive is on its way to gaining a ticket to deep space, since NASA is considering using it in place of Velcro, which creates a lot of dust and bristles that are not particularly welcome in the atmosphere of the International Space Station. At the moment, astronauts are using it to secure objects to internal panels (Ellis, 2016).

Another example of the employment of gecko adhesive technology is the LEMUR 3 robot. LEMUR 3 was built for two projects, one focused on crawling across the exterior of the International Space Station using gecko adhesive end effectors, and one focused on climbing vertical cliffs and traversing cave ceilings on the Moon and Mars using microspine grippers (Parness et al., 2017).

In order to mimic the geckos' setae, it was developed a synthetic gecko adhesive creating 80 µm hairs out of silicone. When the material is placed on a flat surface and sheared in the attach direction (Figure 2.8), the hairs comply to the surface creating a large area of

contact with minimal stored energy. Van der Waals forces cause an attraction between the adhesive and the surface, attaching the gripper. When the gripper is sheared in the detach direction, the hairs are peeled up, real area of contact and van der Waals forces are lost, and the gripper detaches with very low force. In this way, the gecko adhesive can be turned on and off (Parness et al., 2017).

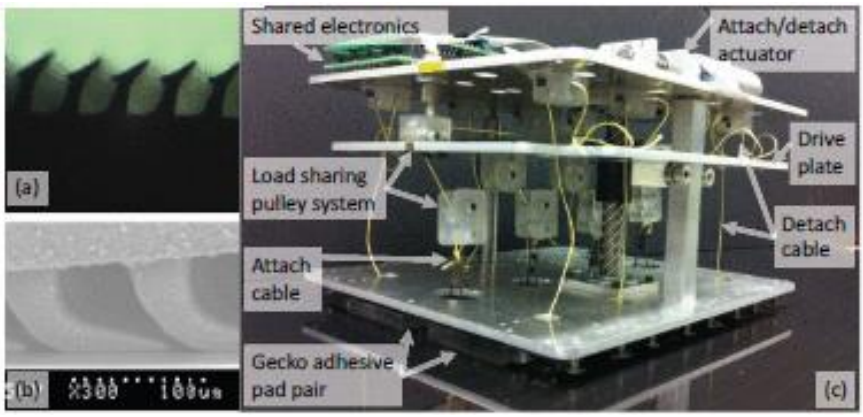

Figure 2.8 – Gecko adhesive in its detached state (a) and its attached state (b). Gecko adhesive gripper (c) attached to a solar panel (Parness et al., 2017).

A problem in this type of materials is that their adhesive performance worsens considerably with dust, high surface roughness, or if the material is wet.

In Figure 2.9 is present an image of the LEMUR 3 been demonstrated climbing on a smooth, flat, clean surface with gecko adhesive grippers.

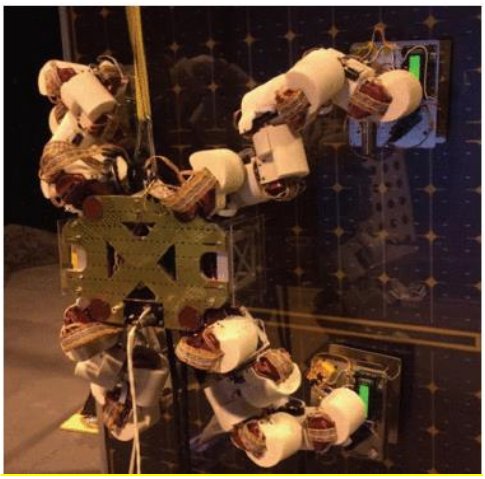

Figure 2.9 – LEMUR 3 climbing on a mock-solar panel surface using gecko adhesive grippers (Parness et al., 2017).

LEMUR 3 gecko adhesive grippers can support a normal load of 150 N using eight 10 cm^2 tiles of adhesive. The tiles are arranged in opposing pairs. Pulling on a cable between the pairs attaches the gripper. Separate cables connected to the back of each pad detach them. A single motor drives both the attaching and detaching cables by moving a plate of pulleys up and down. The pulleys share load equally between the pads (Parness et al., 2017).

It is of noting that, to replicate the reduced-gravity or zero-gravity environment of each mobility scenario, the robot was gravity offloaded during the tests using an overhead constant force spring. Since the grippers are insufficient to support LEMUR 3's mass in Earth's gravity under all conditions (Parness et al., 2017).

Another example is a dry adhesive patch with hierarchy in medical bandages (J. U. Kim et al., 2016).

It was reported mushroom like micropillars used with a commercially available unit of skin patch electrode that can monitor biosignals (Figure 2.10(a)). As displayed in Figure 2.10, a widely used acrylic medical patch has several side effects such as redness, allergic response, and adhesion degradation by repeated attachment/detachment. On the other hand, the dry adhesive skin patch shows reduced pain during peel-off and undesirable side effects even after 48 h of use. Also, the dry adhesive patch has more restorable ability after every five cycles with the help of self-cleaning with water compared with widely used acrylic medical patches (Figure 2.10(c)). Hence, hierarchically bioinspired dry adhesive patches have the potential to be of great benefit in longitudinal biosignal acquisition (J. U. Kim et al., 2016).

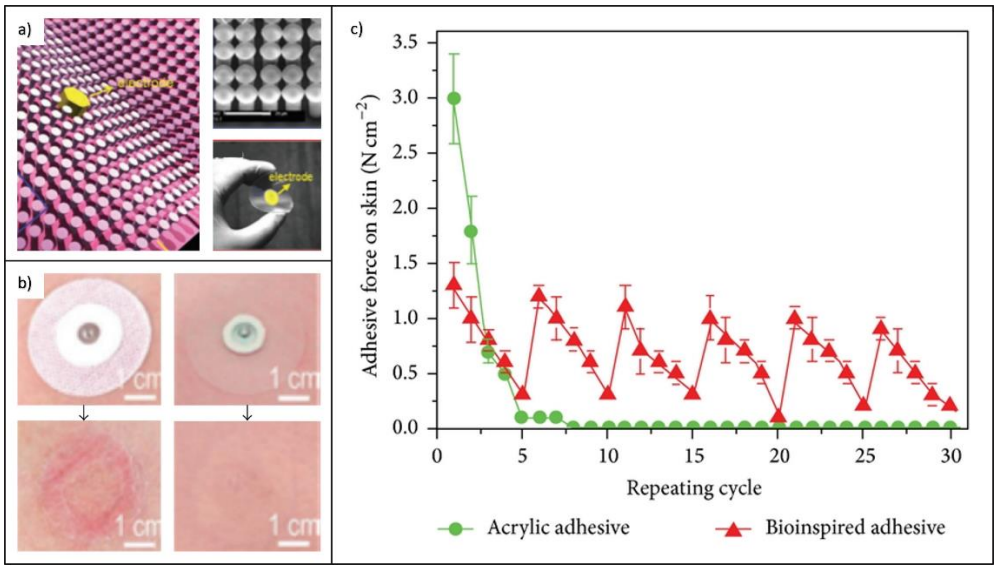

Figure 2.10 – a) Conceptual illustration (left), SEM image (top right), and photograph (bottom right) of bioinspired dry adhesive as medical skin patch; (b) Photographs show the skin condition after use of acrylic adhesive (left) and bioinspired dry adhesive during 48 hours. (c) Variations in normal adhesion strength of acrylic adhesive and bioinspired dry adhesive on the skin with 30 repeating cycles. Both adhesives were cleaned every 5 times (J. U. Kim et al., 2016).

2.4. MICRO/NANOFABRICATION TECHNOLOGIES

Micro/nanofabrication technologies are indispensable for fabricating functional electronic, optical, medical, and biochemical devices. For the fabrication of devices at the micrometer scale, a variety of techniques are used. Some of these techniques have been specifically developed for microfabrication, while others have been adopted from the field of semiconductors.

The main trend has been the use of lithography and microfabrication methods to produce unique molds out of silicon, photoresist, or silicone rubber from which the final dry adhesive products can be cast. These methods are applied sequentially during the microfabrication process to create the desired structure. The patterns can be created either on the substrate's surface, using surface micromachining, or inside the material's body, a process known as bulk micromachining. But for the most part, the intended system is created by combining bulk and surface micromachining (Betancourt & Brannon-Peppas, 2006).

Some of the more important microfabrication techniques are photolithography, soft lithography, film deposition, etching, and bonding.

Photolithography is used to transfer a user-generated shape onto a material through the selective exposure of a light sensitive polymer. Soft lithography encompasses three different techniques which are all based on the generation and utilization of the mold of a

microstructure out of PDMS. Film deposition, as its name suggest, consists of the formation of micron-thick films on the surface of a substrate. Etching selectively removes materials from the surface of the microdevice by either chemical or physical processes. Finally, bonding adheres substrates together with or without the use of intermediary layers (Betancourt & Brannon-Peppas, 2006). Figure 2.11 presents several microstructures manufactured by soft molding.

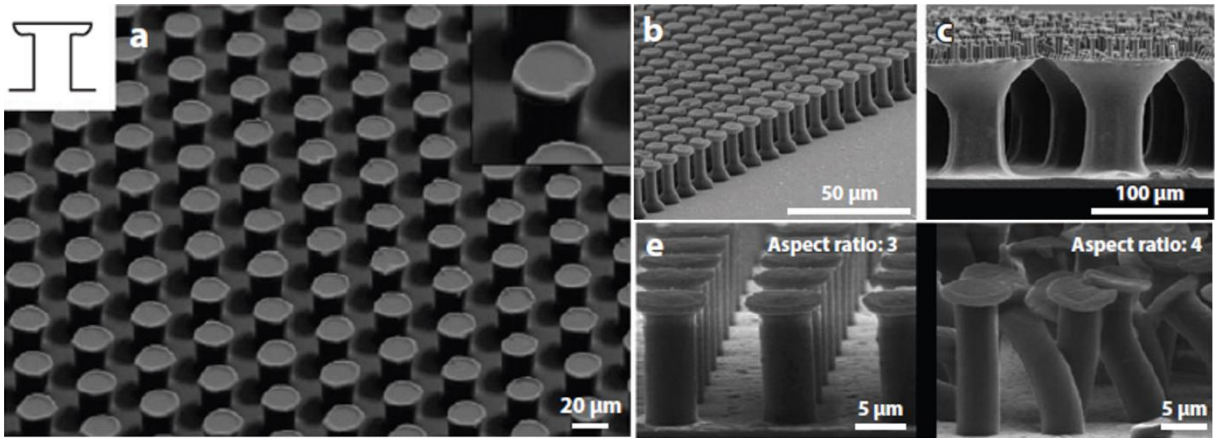

Figure 2.11 – A collection micropillars with mushroom-shaped terminations reported in the literature produced by a soft molding technique (Heepe & Gorb, 2014).

The following section will discuss these and other techniques in more detail.

2.4.1. NANOIMPRINT LITHOGRAPHY (NIL)

The process of nanoimprint lithography (NIL) was first demonstrated by Chou et al. in 1995 (Chou et al., 1995). The concept behind the technology is mechanical duplication, whereby surface reliefs from prepatterned molds are embossed into a thin layer on the substrate.

In the NIL, a resist layer (with thermal or photocurable polymer) is coated on a substrate and then pressed by a rigid mold with patterns at 1: 1 scale through mechanical contact. The resist layer is cured with pressure by thermal or UV curing known, respectively, as temperature-based processing and light-initiated polymerization (J. U. Kim et al., 2016).

NIL can duplicate any designs on a variety of substrates since, in theory, it has no pattern geometry restrictions. As a result, NIL can fill the gap between manufacturing at the production level and laboratory-level investigations of nanobased techniques.

Figure 2.12 represents a schematic of the fabrication of re-entrant polymer structures by UV-NIL.

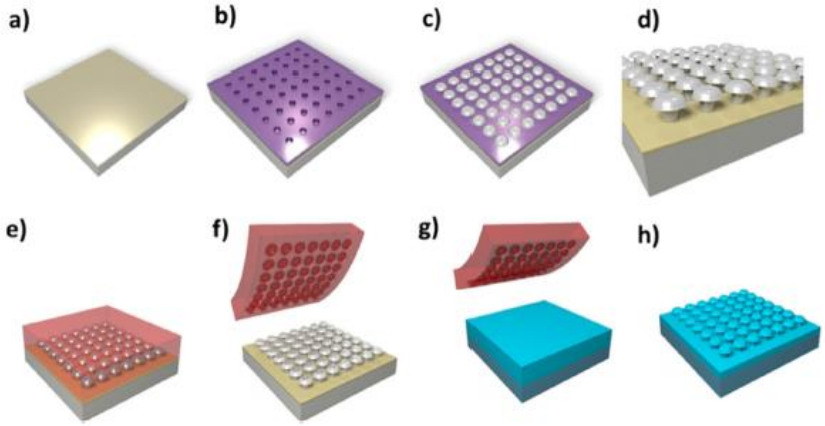

Figure 2.12 – [(a)–(h)] Schematic of the fabrication process followed to develop the polymeric mushroom-shaped structures. The template was fabricated on nickel by electrodeposition [(a)–(d)]. A soft stamp was produced with the negative pattern [(e) and (f)]. This soft stamp was used to produce mushroom-shaped structures by direct UV-NIL [(g)–(h)] (Kehagias et al., 2018).

However, in this work NIL cannot be used since this process usually works with dimensions below 1 µm and as will be shown later it will be necessary to insert particles up to 5 µm in the structures to be fabricated.

2.4.2. PHOTOLITHOGRAPHY AND REPLICA MOLDING

The paper Y. Wang et al. (2014), presents a method for fabricating mushroom-shaped structures utilizing conventional photolithography and molding.

Firstly, a masked and a maskless exposure are performed on the top and bottom of a photoresist, respectively, that generates microholes with an undercut after development. This structured photoresist is then used for molding, leading to mushroom-shaped structural features after sacrificing the photoresist.

In Figure 2.13, it is shown a fabrication procedure for mushroom-shaped micropillars. This process initiates with the spin-coating followed by soft baking of a photoresist. Then, a UV light is passed through a mask from the top side and the exposure dosage is adjusted to ensure a complete exposure of the photoresist. In addition, the UV light irradiates the back side, and the photoresist is exposed for a short time without any masking so that only a thin layer is completely exposed.

Afterwards, PDMS is used as a filling material to duplicate the structures from the template. As cured, the PDMS does not dissolve in ethyl alcohol, but the photoresist does so

PDMS pillars with mushroom-shaped tips can be easily obtained in ethyl alcohol (Y. Wang et al., 2014).

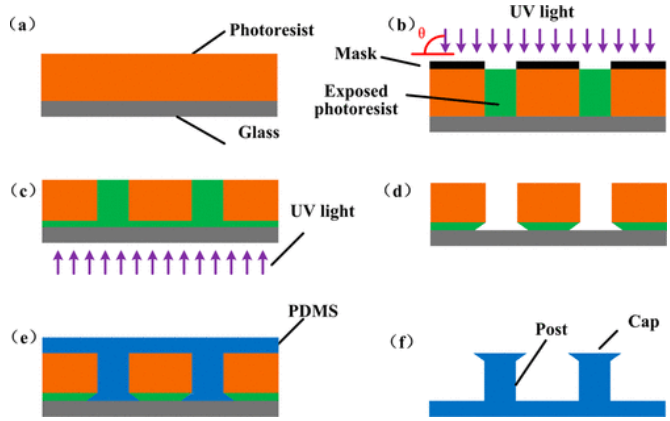

Figure 2.13 – Schematic diagram of the processing steps for fabrication of mushroom-shaped micropillars. (a) Photoresist spin-coating and baking. (b) Photoresist exposed from top side with a mask present. (c) Flooding exposure from substrate side without any mask. (d) Photoresist is developed, leaving undercut holes. (e) Sylgard 184 is mixed then poured on the mold and cured. (f) The cured silicone is demolded, leading to mushroom-shaped pillars. (Y. Wang et al., 2014).

In the work of Wang et al. (2017) it is also used photolithography for the fabrication of mushroom-shaped microstructures.

In Figure 2.14 is illustrated the process flow for creating mushroom-shaped microstructures, in which it is used double photolithography and cast molding.

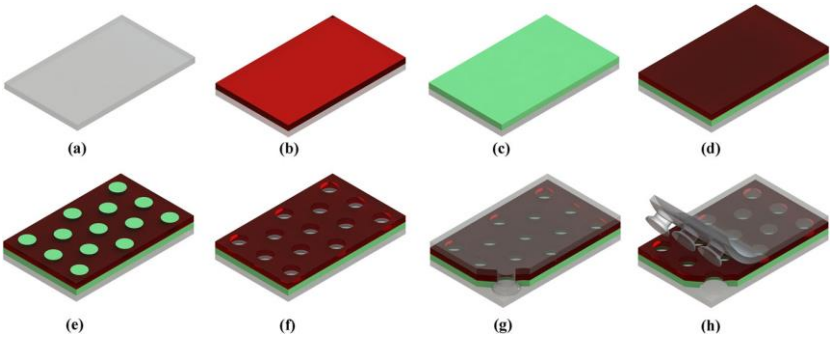

Figure 2.14 – Schematic representation of the processing steps for fabrication of arrayed mushroom-shaped microstructures:(a) substrate cleaning, (b) photoresist spin-coating and pre-baking, (c) flood exposure, (d) second layer of resist coating and baking, (e) photolithography, (f) development and post-baking, (g) cast molding with PDMS, and (h) cured PDMS demolding(L. Wang et al., 2017).

2.4.3. UV IMPRINTING

Figure 2.15 shows the details of the UV imprinting processes. The PET is placed manually on the center of a stage in the chamber to lay the pattern area of PDMS mold on the resin-coated area during the next process. The PDMS mold was fixed to a motor that could have its

vertical movement controlled from outside the chamber. After the mold is placed into contact with the UV-curable resin (b). Then, the mold with the resin and PET substrate is pressed by rotating a roll from above(c). Then, the resin was cured by UV light irradiation without any load (d). Finally, the mold was peeled off manually along a roll with a diameter of 60 mm (e). This process is called the roll press method (Shinohara et al., 2013).

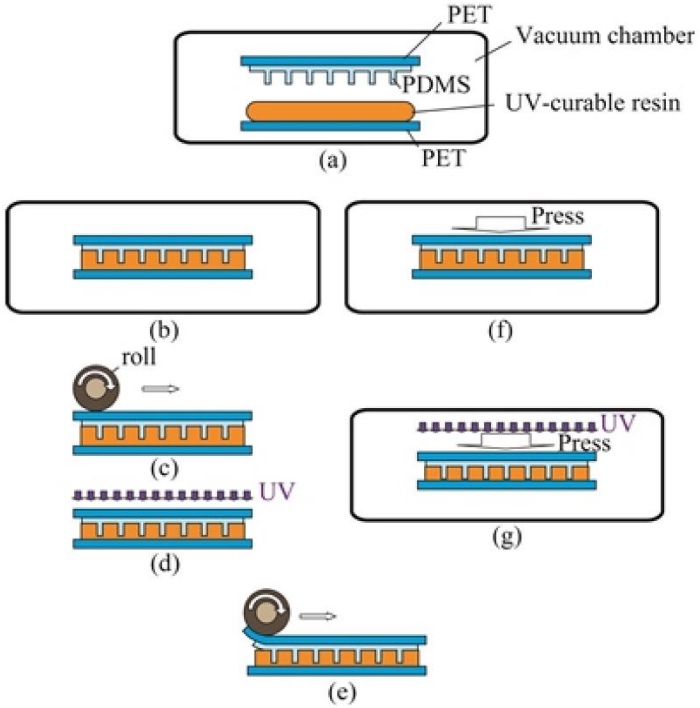

Figure 2.15 – UV imprinting process: (a) placing PDMS mold and UV-curable resin-coated polyethylene terephthalate (PET) in a vacuum chamber; (b) moving mold and resin into contact under reduced pressure; (c) pressing by rotating roll; (d) UV irradiation; (e) peeling off mold along roll; (f) pressing mold and resin under reduced pressure; (g) UV irradiation and pressing. The roll press method includes (a), (b), (c), (d) and (e), and the batch press method includes (a), (f), (g) and (e)(Shinohara et al., 2013).

The roll press method is expected to be applied to fabricate larger area high aspect ratio structures that are suitable for mass-production.

2.4.4. DOUBLE MOLDING

Microfabrication techniques have a very specific materials selection that can be expensive, and patterning can only be carried out in specialized laboratories that require costly equipment and long processing times. Also, the type of microfabrication used needs to take into account the size of the particles that are intended to mix with the PDMS. Therefore, it was looked for an alternative fabrication process technique.

Using a double molding technique, researchers reproduced the 3D printed structure in PDMS elastomer. The 3D-printed positive structure was initially duplicated as a negative in an elastomer called Ecoflex 0030. For the 3D printed replica, PDMS Sylgard 184 was then cast and hardened in the negative Ecoflex mold (Sharma et al., 2021a).

An alternative method, involving 3D printing the negative mold first and then casting the PDMS on it, is ineffective for two reasons: it is generally difficult to print negative molds with complex 3D features by means of the printers in use and small features on the PDMS have a tendency to break while being peeled off the 3D printed mold.

Consequently, the use of double molding is required. A crucial material to this process is the Ecoflex, since it is a softer elastomer than PDMS and can be stretched up to nine times its original length, making it simpler to demold the PDMS.

2.5. MAGNETORHEOLOGICAL ELASTOMERS (MRES)

The combination of magnetic microparticles and an elastic soft polymeric matrix makes it possible to obtain an intelligent material with a wide range of tunable properties. These composites are known as magnetorheological elastomers (MREs). The principal effect of a magnetic field on these composites is a change in their viscoelastic properties (Borin & Stepanov, 2022). The magnetorheological (MR) effect is a term used to describe this change in attributes. The MR impact depends on a number of variables, including the type of matrix materials, the kind, concentration, and distribution of magnetic particles, the usage of additives, operating modes, and magnetic field strength (Bastola & Hossain, 2020).

Figure 2.16 lists the essential components of an MRE composite. A nonmagnetic polymeric matrix filled with magnetizable particles of different fractions and additives makes up an MRE material.

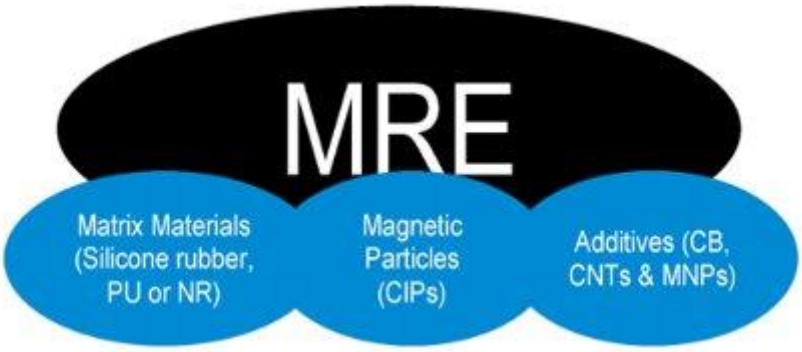

Figure 2.16 – Main constituents of MREs (Bastola & Hossain, 2020).

The mechanical characteristics of MREs, including initial modulus, field-dependent modulus, and MR effect, are greatly influenced by the choice of matrix material. Silicone rubbers, vinyl rubbers (VR), polyurethanes (PU), thermoset/thermoplastic elastomers, and natural/synthetic rubbers have all been used as matrix materials in the production of MREs. However, among other polymers, silicone rubbers are the most frequently utilized ones. They are appealing in MRE applications due to the unusual features they possess. For instance, silicones are easily accessible in their resin (liquid state), which makes it easier to suspend the magnetic particles uniformly throughout the manufacturing process.

The magnetic field dependent features of MREs are mostly caused by magnetic particles, which are field sensitive components of MREs. The magnetizable particles that are employed the most frequently are carbonyl iron powders (CIPs). Because of their softness, high magnetic permeability, low magnetic remnant, and high magnetic saturation, CIPs are regarded as one of the finest options for producing MREs. Additionally, it has been thought about using magnetic particles like iron sands, nickel, and cobalt to create MREs.

The additional elements in MREs are called additives. Enhancing magnetic field-dependent characteristics is the main benefit of additions in MREs. Additionally, taking into account additives in MREs opens up new possibilities for MRE-based applications by providing sensing and actuation capabilities like a change in capacitance and resistance. In MREs, additives are divided into magneto-active and nonmagnetic categories. Non-magnetic additions include silicone oils, plasticizers, and substances based on carbon, while magnetic additives include magnetic nanoparticles (MNPs), nanorods made of Fe_2O_3, and chromium-based particles. Silicone oil, mineral oil, phthalate easters, and silicone/natural-based easters are the most widely used additives, or plasticizers. These plasticizers are combined with matrix

components that aid to increase flexibility, flowability, and workability, hence facilitating the processing of MRE materials (Bastola & Hossain, 2020).

2.6. CLASSIFICATION OF ADHESION TESTS

Usually experiments investigating the adhesion of these patterned surfaces press flexible fibrils against a stiff spherical substrate or a flat surface with predefined roughness and the adhesive strength is then evaluated during subsequent tensile loading.

The probe is brought in contact with the sample, applying a predetermined compressive load (preload) perpendicular to the sample surface; then is retracted while the force and displacement are measured.

In Figure 14.1 a schematic of three classifications of adhesion tests is shown, according to the direction of the force measured during the experiment relative to the sample surface. These being (Kamperman et al., 2010a):

(a) Normal adhesion: application of a tensile load normal to the sample surface, force and deflection are measured parallel to normal preload.

(b) Shear (or friction) test: the sample is moved tangentially to the sample surface, force and deflection are measured perpendicular to normal preload.

(c) Peel test: sample is peeled from one end of the substrate under a defined angle.

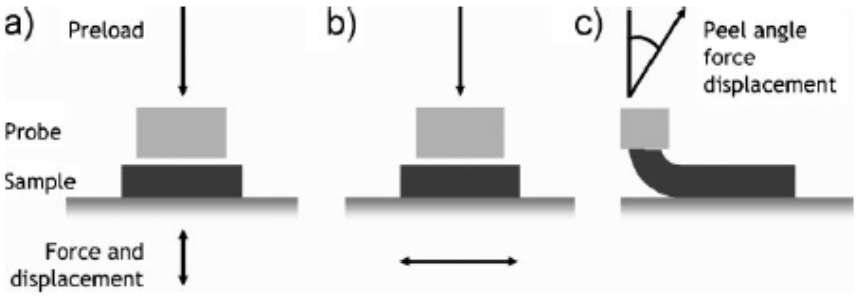

Figure 2.17 – Schematics of adhesion tests. a) Normal adhesion test; (b) Shear (or friction) test; (c) Peel test (Kamperman et al., 2010a).

3. MATERIALS, EQUIPMENT AND METHODS

The materials, equipment's, and methods employed during the current study are described in this chapter. First, the materials will be mentioned (PDMS, silane, Ecoflex, carbonyl iron particles). After that, the equipment used for the fabrication and characterization of the microstructures will be explained (laser cutter, CNC, 3D printer, plasma oven, UTM, optic microscope).

Still in this chapter can be found the analytical evaluation of the adhesion mechanism.

3.1. MATERIALS

3.1.1. POLYDIMETHYLSILOXANE (PDMS)

The PDMS Sylgard™ 184 produced, and it consists of two parts, a silicon base, and a curing agent.

This polymer is the most popular silicon-based organic, which is distinguished by its special abilities to cure at low temperatures, rapid curing at high temperature, deformation reversibility, and have controllable surface chemistry using processes reasonably well developed (Tian et al., 2013b). The surface properties of PDMS are also relatively easy to modify.

PDMS is one of the most widely used materials for the fabrication of gecko inspired adhesives. PDMS has a Poisson's ratio close to 0,5 and a Young's modulus ranging from approximately 100 kPa to approximately 10 MPa, depending on the amount of crosslinking that is, the ratio between the silicon base and the curing agent (Balijepalli et al., 2016).

In general, PDMS is regarded as inert, non-toxic, and non-flammable and is optically transparent. Prior research has concentrated on the PDMS's structural properties and its kinetic characteristics when crystallizing from solution (Tian et al., 2013b).

It has been reported that tensile testing of bulk PDMS up to a strain of 40% yielded a linear correlation between the elastic modulus and operating temperature, but that applied strain rate had little influence on the measured mechanical properties (Johnston et al., 2014).

The vast majority of reported of microfluidics and microengineering applications of PDMS do not employ standard curing temperatures or durations in their fabrication, and

hence the processing-dependent variation in mechanical properties of the PDMS is poorly understood.

In Table 3.1 above are the curing times and temperatures that have been adopted in various papers.

Table 3.1 – PDMS, Sylgard 184

Ratio (weight or volume)	Time	Temperature	Ref
10:1	24 hours	23°C	(*Dow Corning 184 Sylgard Silicone Elastomer*, n.d.)
	4 hours	65°C	(*Dow Corning 184 Sylgard Silicone Elastomer*, n.d.)
	1 hour	100°C	(*Dow Corning 184 Sylgard Silicone Elastomer*, n.d.)
	5 hours	70°C	(Sharma et al., 2021b)
	10 hours	60 °C	(Chai et al., 2019)
	10 hours	80 °C	(Chai et al., 2019)
	1 h	120 °C	(Zhao et al., 2019)
	35 min	100 °C	(Tian et al., 2013a)
	2 hours	80 °C	(Vaicekauskaite et al., 2020)
	1 h	90 °C	(Drotlef et al., 2014)
	1 h	90 °C	(Drotlef et al., 2014)
	1 h	85 ◦C	(M. Kim et al., 2013)
5:1	30 min	85 ◦C	(M. Kim et al., 2013)
5:1; 7:1; 10:1; 16.7:1; 25:1; 33:1	1 h30	65 ◦C	(Z. Wang et al., 2014)

3.1.2. ECOFLEX

The silicone Ecoflex 00-30 is a very soft and very strong rubber that is used in this work to produce negative molds. It has an elongation at break of 900%, stretching many times its original size without tearing and will rebound to its original form without distortion. It also presents negligible shrinkage (< .0254 mm/mm) making it standard for casting ("EcoflexTM Series," n.d.).

These characteristics are especially suited for the demoulding of the PDMS microstructure from the Ecoflex mold, as the mold elongates around the PDMS allowing the PDMS to demould without breaking in the process.

To produce molds in Ecoflex 00-30 it needs to be weighing of the Ecoflex 00-30 part A and part B, in a ratio 50:50 w/w for approximately 10 minutes.

The Ecoflex curing parameters are shown in Table 3.2.

Table 3.2 – Ecoflex curing parameters.

Ratio (weight or volume)	Time hours	Temperature	Ref
1A:1B	2 h + 2 h	At room temperature + At 70°C	(Sharma et al., 2021b)
	2 h	80°C	(EcoflexTM 00-30, 2022)
	1 h	100°C	(EcoflexTM 00-30, 2022)

3.1.3. TRICHLORO(1H,1H,2H,2H-PERFLUOROOCTYL)SILANE (PFTOS)

Trichloro(1H,1H,2H,2H-perfluorooctyl)silane (PFOTS) is a chlorosilane that forms a self-assembled monolayer (SAM) on a variety of substrates. It is majorly used to modify the surface with superhydrophobic properties. It is a biocompatible polymer with low surface energy (*Sigma-Aldrich*, 2022).

The anti-fouling and high wettability of PFOTS aid in the ability to release different composites from the mold, resulting in it being chosen for use in the double molding process.

PFOTS is a coupling agent that is used to silanize the substrate for the fabrication of microfluidic devices using soft lithography. It can also be used on silicon base that forms a chemically patterned surface for quantitative analysis of insoluble surfactants in the polymeric matrix. Alumina membranes can be treated with PFOTS for the formation of superhydrophobic polyimide (PI) based nanotube arrays (*Sigma-Aldrich*, 2022).

PFTOS was purchased from Sigma Aldrich/Merck.

3.1.4. CARBONYL IRON PARTICLES (CIP)

Magnetic particles were also used to create the MREs in addition to the polymeric matrix. Carbonyl iron particles (CIP) were employed for this project.

Due to their high magnetic saturation, low magnetic remanence, and high magnetic permeability, as well as the fact that they are soft magnetic particles without magnetic hysteresis, carbonyl iron particles are the most frequently used magnetizable particles in the synthesis of MREs.

In Figure 3.1 can be observed that the particle size range is from 800 nm to 5 µm. The particles are about spherical in shape and their sizes are uniform.

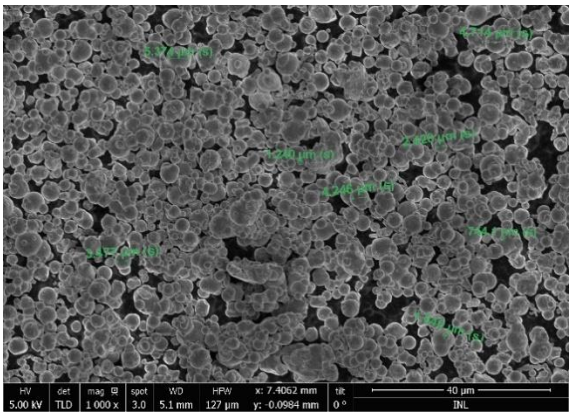

Figure 3.1 – SEM images of the carbonyl iron particles (Pereira, 2022).

The particles were purchased from Sigma-Aldrich. The particles have a density of 7.86 g/cm^3 (Pereira, 2022). The carbonyl iron is an iron powder with an average particle size of 5 to 9 µm.

3.2. EQUIPMENT

3.2.1. LASER CUTTER

For the manufacture of molds for the characterization of mechanical properties the Laser cutter *Widlaser LS1390 Plus* (Figure 3.2) was employed.

Figure 3.2 – Laser cutter *Widlaser LS1390 Plus*.

Laser cutting is a method of cutting shapes or designs into sheet metal or other structural materials. The laser cuts, burns, melts, and then blows away the pattern, as instructed by a computer. The laser beams are easily manipulated to achieve the desired result.

3.2.2. CNC – High Speed Milling System

The High Speed Milling System was used during this work for the fabrication of molds for the characterization of mechanical properties and for the manufacture of flat cylindrical pillars. The CNC used was the *FlexiCam Viper* (Figure 3.3), a CNC 3-axis tool that allows the machining of pieces up to 650x650x280 mm and allows the machining of different materials (like plastics, glass, and metals) in a controlled and precise way.

Figure 3.3 – CNC (3 axis tool) FlexiCam Viper, allows the machining of pieces with size up to 650x650x280 mm, and has a fixed gantry (moving table design for maximum stiffness and high accelerations).

Tools for High Speed Machining (Peak, 2022):

- Use Dedicated Tools: It is important to have dedicated roughing and finishing tools in order to reduce tool wear between separate operations.
- Keep Tooling Short: Machine tools are pushed to their limits for HSM. In order to obtain high accuracy, repeatability, and surface finish, fixtures and tools must be absolutely rigid to withstand the high loads associated with the process.
- Balanced Tooling: Tool balance is important when running at high RPMs. Most common tool designs with tool holders will work without a noticeable problem at speeds less than 7,000 to 8,000 RPM. But, at higher speeds, you can start to see runout problems and decreased tool life. Shrink fit tooling is essential in order to maintain balance at high RPM.
- A Clean Process: High Speed Milling generates chips faster than conventional milling. Use oil mist/air blast, or coolant (when necessary) in order to clear chips away to an appropriate chip management solution.

3.2.3.3D PRINTER

In this work, the *Form 2* stereolithography (SLA) 3D printer (Figure 3.4) from Formlabs was used for the fabrication of the positive molds of the microstructures. This 3D printer uses a laser to cure solid isotropic parts from a liquid photopolymer resin (photopolymerization). It delivers high-resolution parts at a lower cost and footprint of industrial 3D printers. The minimum feature that can be made is 140 µm and the layer can go from 25 to 100 µm of thickness.

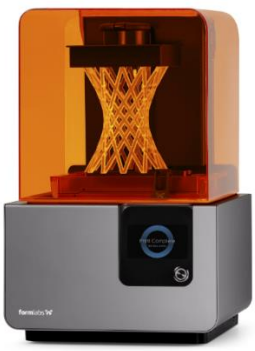

Figure 3.4 – SLA 3D printer used for the printing of microstructures positive molds (Manufacturer: Formlabs; Model: *Form* 2).

To prepare the 3D models for printing, is used the software *PreForm*. The software offers print setup with manual controls to adjust support parameters, layer thickness, and functions to save material and time.

There are several resins that can be used on this machine, all with different properties and different performance levels. Some engineering resins materials can be soft others hard or imbued with mechanical properties like high heat deflection temperature or impact resistance.

The one used in this work was the grey resin. This resin produces prints with high stiffness and high-resolution. The grey resin is ideal for fabricating parts with fine details, concept modeling and rapid prototyping. This resin has a low cost which makes it ideal for prototyping applications. However, it has low elongation at break, low impact strength and low heat deflection temperature ("SLA 3D Printing," n.d.).

The SLA printed parts need to be post-processed after printing. First, to remove extra resin, the parts must be washed in a solvent, process which is automated, Figure 3.5. Next, the pieces must undergo post-curing (60 minutes at 65 degrees Celsius).

Figure 3.5 – Automated washing of printed pieces.

Because the 3D printed parts are printed on supports, it is required to remove/cut these manually. Followed by the sanding of the parts in contact with the supports.

3.2.4. PLASMA CLEANER

The *Plasma Cleaner PDC-002* (Figure 3.6) was used to perform the plasma activation of the 3D printed and micropatterned Ecoflex molds. This instrument is a benchtop plasma instrument, used for nanoscale surface cleaning and surface activation. It has a chamber with

a diameter of 15.24 cm and a length of 16.51 cm. It's maximum RF (radio frequency) power is 30 W.

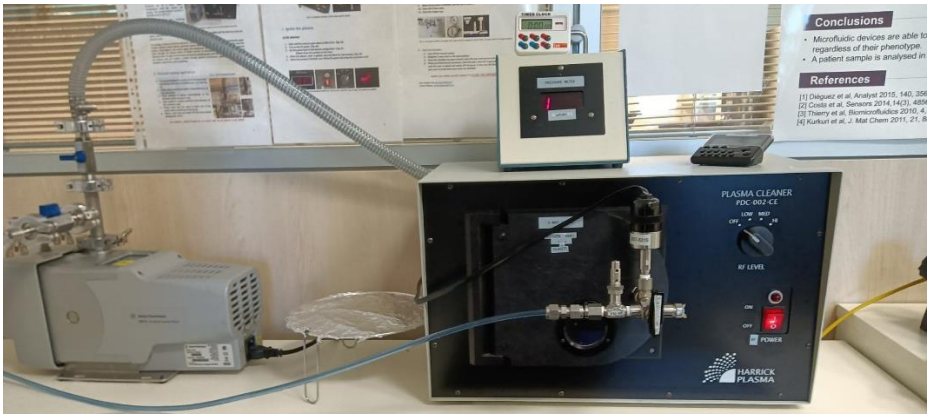

Figure 3.6 – Plasma Cleaner unit in the microfluidics lab at INL, used for nanoscale surface cleaning and surface activation. On the left, is seen the vacuum pump (Agilent IDP-3 dry scroll pump) required by the plasma cleaner to achieve determined vacuum pressures.

The vacuum pump Agilent IDP-3 dry scroll pump is used to pressurize the chamber, it is used the vacuum pump Agilent IDP-3 dry scroll pump. The IDP-3 is a compact, hermetic, oil-free vacuum pump suitable for pumping air or inert gases ("IDP-3 Dry Scroll Vacuum Pump," n.d.).Plasma is generated when a radio frequency (RF) oscillating electric field is generated in the gas region, either through the use of capacitive plates or through magnetic induction. This RF at sufficient low pressures leads to heating of the electrons. When electrons gain kinetic energy in excess, electron neutral collision leads to further ionization, yielding additional free electrons that are heated in turn.

The energy of plasma electrons and ions is sufficient to ionize neutral atoms, break molecules apart to form reactive radial species, generate excited states in atoms or molecules, and locally heat the surface. Depending on the process gases and parameters, plasmas are capable of both mechanical and chemical work, through the interaction of reactive radical species with the surface. In general, plasmas can interact with and modify a surface though several mechanisms: ablation, chemical etching, activation, deposition, and crosslinking.

Plasma cleaning removes organic contaminants by chemical reaction (O_2 or air plasma) or physical ablation (Argon plasma). Plasma treatment also introduces chemical functional groups (carbonyl, carboxyl, hydroxyl) on the surface, rendering most surfaces hydrophilic. This is observed as a decrease in water contact angle and increased wettability. A clean, as well as hydrophilic surface, is often critical to promote adhesion and enhance bonding to other

surfaces (*PLASMA PROCESS GASES*, n.d.). In this work the plasma cleaner is used to perform surface activation.

3.2.5. OPTICAL MICROSCOPE

In order to perform an inspection on the developed microstructures the optical microscope *Eclipse L200N* (Figure 3.7) was used.

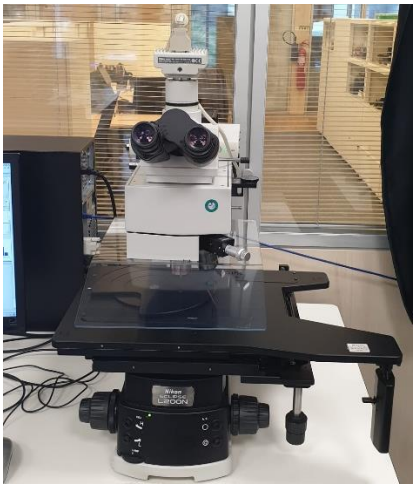

Figure 3.7 – Optical microscope Eclipse L200N.

This microscope offers images with excellent contrast, high resolving power, and darkfield images when combined with Nikon's optical system and an illumination system. The L200 series performs precise optical inspection of wafers, photo masks, reticles, and other substrates when used individually or in conjunction with wafer loaders.

3.2.6. UNIVERSAL TESTING MACHINE (UTM)

The UTM Shimadzu AGX-V 10 kN (Figure 3.8) was employed to conduct the experimental tests.

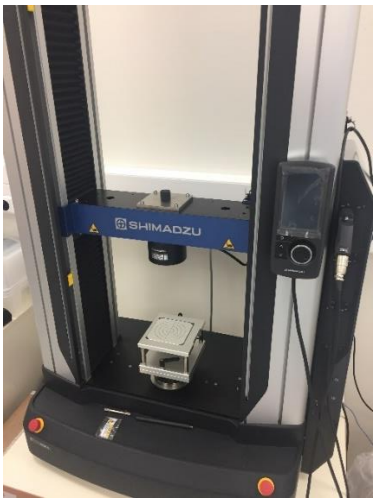

Figure 3.8 – The Shimadzu AGX-V 10 kN is a precision UTM (universal testing machine) to perform destructive tests and/or measure strength property of materials.

The Universal Testing Machine (UTM) has a smart controller with a progressive user interface, a crosshead with intelligence, stroke limit switches, high-speed sampling, high-accuracy automatic control, software that allows the construction of test conditions, and software that supports data processing. The instrument can function with various load cell, a load cell of 500 N was used in this work, capacities and has a large range of accessories. It has a test force measurement accuracy within ±1 % of indicated test force (for forces ranging from 1/1000 to 1/1 of the load cell capacity rating).

Characterization of the PDMS

To the characterization of the PDMS, the specimens were put through a tensile test on a Universal Testing Machine SHIMADZU in accordance with the ASTM D412 standard (Thackeray, 2022). A guideline used for assessing the tensile characteristics of thermoplastic elastomers and vulcanized rubber.

In accordance with the standard, the test is performed at a velocity of 500 mm/min, until the sample rupture. To make sure the samples were tensed, it was also performed a pre-test a speed of 5 mm/min until a load of 1 N was reached.

As shown in Figure 3.9, the clamps were used to secure each sample in its wide region. When the tests were first conducted, it was discovered that the PDMS samples would move from its clamps. Four sheets of fine particle sandpaper were attached to the surface of samples for better fixation.

Figure 3.9 – Tensile testing of PDMS specimen.

The compression testing of the PDMS samples was carried out using the Shimadzu universal testing equipment, according to ASTM D1229-03 (Figure 3.10). The test's speed was set at 20 mm/min.

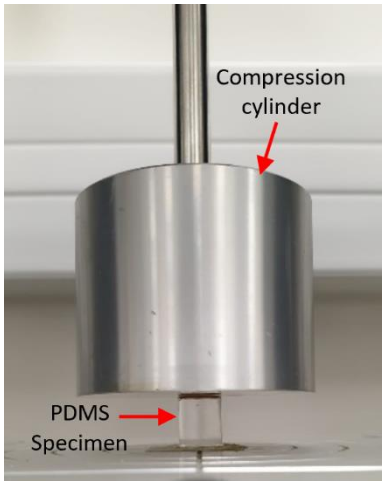

Figure 3.10 – Compression testing of PDMS specimen. A compression cylinder compresses the PDMS specimen until rupture, at a predetermined speed.

During compressive tests, the specimens are known to experience the barrel effect as the applied force rises. In order to prevent this barrel effect on the compression specimen, a drop of machine oil was applied to the sample's surface (the one that meets the compression cylinder) before each test. Despite this, the samples were still barreled.

Adhesion Experiments

The adhesion experiments can be divided in two parts. In the first part, the pillar is compressed until it reaches a determined applied force. In the second part this force is removed.

In Figure 3.11 it can be observed the set up prepared for the execution of these experiments.

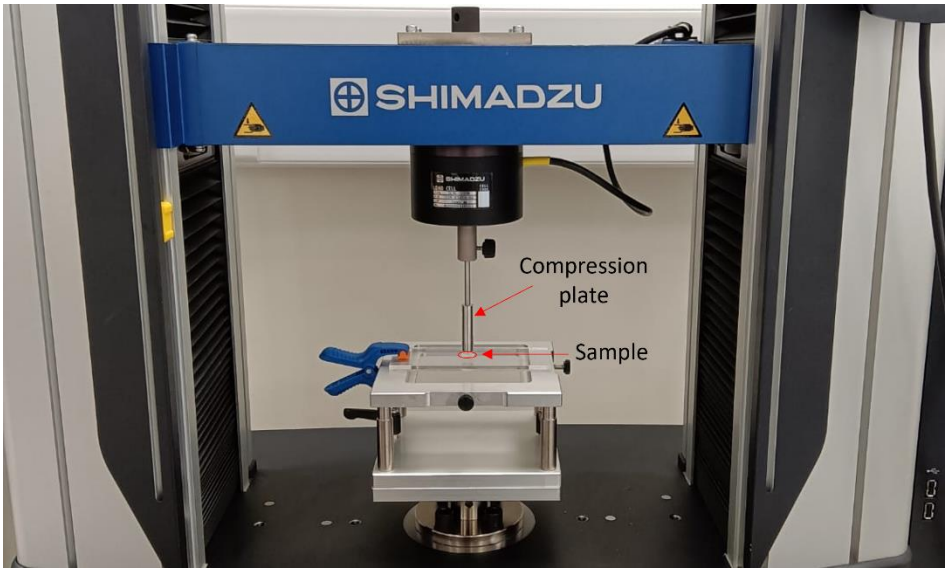

Figure 3.11 – Set-up prepared for the realization of the adhesion tests.

In the adhesion tests a stroke of 4 mm/min was parameterized until the pillar reached the applied force, at which point, the force that is being applied is held for 3 seconds. After, the deformation is removed until the compression plate achieved a force of -1N or the pillar completely detach from the compression plate.

The data is extracted from the UTM and treated and analyzed on MATLAB ®.

3.3. METHODS

3.3.1. ANALYTICAL EVALUATION OF THE ADHESION MECHANISM

Several studies have highlighted the importance of optimizing the distribution of interfacial stresses in order to achieve high adhesion. It also has frequently been shown that fibrils with tips in the shape of mushrooms display greater adhesion performance (del Campo et al., 2007; Gorb et al., 2007; Greiner et al., 2007).

Matching numerical simulations, the main cause of the increased adhesion is the decreased stress magnitudes associated with the corner singularity, which is anticipated to serve as the starting site for cracks in straight homogeneous punch (SHP) fibrils (Khaderi et al., 2015). The edge stresses in mushroom fibrils were numerically demonstrated to be considerably lower than those in SHP and other shapes (Balijepalli et al., 2017; Spuskanyuk et al., 2008).

Work based on the corner stress singularity, addressed the stress distributions of mushroom fibrils., and it showed that such structures distribute tractions along the interface and reduce the magnitude of the stresses associated with the singularity at the corner. This is suggested to be the main cause of the higher adhesion of mushroom structures while the onset of detachment is shifted away from the corner to the center of the interface (Balijepalli et al., 2017).

In this work it is followed the approach of Balijepalli et al., 2016 to describe the corner stress singularity towards explore the mechanics of detachment of 2D and 3D fibrils.

The corner stress singularity is considered to occur at the edge of a properly bonded, compliant mushroom fibril on a rigid substrate, where sliding of the fibril relative to the substrate is prohibited. Figure 3.12 depicts compliant fibrils attached to a hard substrate.

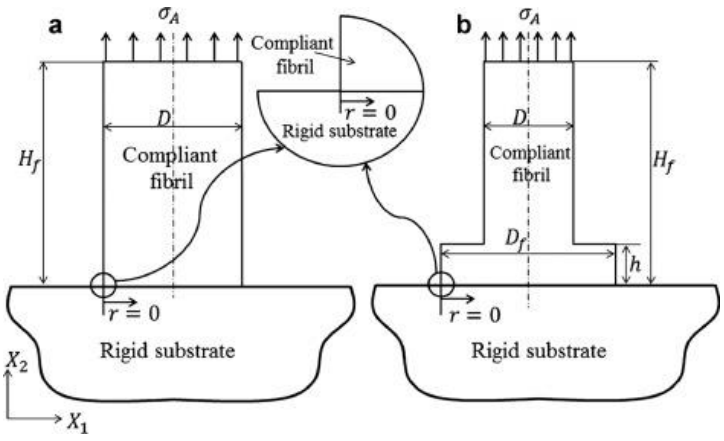

Figure 3.12 – Schematics of (a) a straight punch shaped fibril without a mushroom cap (SHP) and (b) a fibril with a mushroom cap, both adhered to a rigid substrate (Balijepalli et al., 2016)

Analytical solution for the corner singularity

In this analysis it is considered a compliant fibril adhered to a rigid substrate without any interfacial crack. The fibril is treated as an incompressible, isotropic elastic solid, and the edge of the fibril always meets the substrate at right angles.(Balijepalli et al., 2016)

Using the method adopted by (Balijepalli et al., 2016), the most singular terms in the asymptotic normal (σ_{22}) and shear (σ_{12}) stress components along the interface between a compliant fibril and a rigid substrate are (Balijepalli et al., 2016):

$$\sigma_{22} = H_1 . r^{-0,406}, \tag{3.1}$$

$$\sigma_{12} = 0,505 . H_1 . r^{-0,406}, \tag{3.2}$$

Where *r* is the distance from the fibril edge and is the amplitude of the singularity.

Application of an axial stress to the free end of the pillar results in a singularity in stress at the corner with the substrate.

The amplitude of the singularity H_1 can be written in terms of the applied stress and one relevant dimension of the fibril and a calibration coefficient *ã*. Choosing the average stress σ_1 on the interface between the fibril and the substrate as the measure of the applied stress and the width or diameter, D_f, of the mushroom flange as the relevant dimension and obtain:

$$H_1 = \sigma_1 . {D_f}^{0,406} . \tilde{a}, \tag{3.3}$$

The parameter *ã* controls detachment processes at the edge of fibril and that a low value is beneficial for good adhesion.

The average interface stress (σ_1) for a plane strain (2D) slab is:

$$\sigma_1 = \sigma_A . \frac{D}{D_f}, \tag{3.4}$$

And for axial symmetry (3D) is:

$$\sigma_1 = \sigma_A . \left(\frac{D}{D_f}\right)^2 \tag{3.5}$$

Where σ_A is the stress applied to fibril stalk.

In the case of a straight punch without a mushroom cap:

$$D_f = D, \tag{3.6}$$

$$\sigma_1 = \sigma_A, \tag{3.7}$$

$$\tilde{a} = a_1, \tag{3.8}$$

According to Khaderi et al., 2015:

$$a_1 = 0{,}331, \tag{3.9}$$

$$a_1 = 0{,}278\,, \tag{3.10}$$

Adhesive strength

In order to predict the adhesive strength of the fibril, it is assumed that there is a small detachment or defect of length *l* at the edge of the fibril as seen in Figure 3.13.

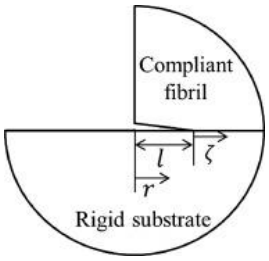

Figure 3.13 – Schematic of a small crack along the interface at the corner of the contact (Balijepalli et al., 2016).

The energy release rate (G), according to (Balijepalli et al., 2016), upon detachment is given by:

$$G = \frac{1-\nu^2}{2E}\,(K_I^2 + K_I^2) = \frac{3}{8E}\,(K_I^2 + K_I^2), \tag{3.11}$$

$$G = \frac{2{,}8\,{\sigma_1}^2.{D_f}^{0{,}81}.l^{0{,}19}.\tilde{a}^2}{E}\,, \tag{3.12}$$

Where ν is the material Poisson's ratio, equal to 0,5 consistent with incompressibility (Balijepalli et al., 2017).

For detachment initiated at the edge, the energy release rate is equal to the adhesion energy, W. The adhesion strength of the composite fibril S' can be expressed as

$$S' = \frac{0{,}6\sqrt{E.W}}{{D_f}^{0{,}406}.l^{0{,}094}.\tilde{a}}\,, \tag{3.13}$$

To define a normalized adhesion strength, the adhesion strength of the composite fibril S' is divided by the value for the straight homogeneous punch S_{punch}, given that these elements are assumed to have the same initial crack length (Balijepalli et al., 2017):

$$\frac{S'}{S_{punch}} = \frac{a_1}{\tilde{a}}, \tag{3.14}$$

From the previous equations is observed that as the mushroom cap diameter is increased and as the cap thickness is decreased, the adhesive strength rises. The fibril cap geometry plays an important role in promoting adhesive strength.

It can be concluded that (Balijepalli et al., 2016):

- Both a thin mushroom cap and one with a large diameter enhance the adhesive strength of the fibril when strength is controlled by detachment from a defect at the corner.
- The adhesive strength can be enhanced by 10 orders of magnitude over the straight punch strength (S_{punch}) when the mushroom cap diameter is twice that of its fibril stalk and its thickness is less than 1% of its diameter.

Critical force

In addition to the previous equations, Euler's formula provides an appropriate equation to calculate the critical load on the fibrils.

Vertical pillar with radius R = D/2 has an aspect ratio AR (L/R) equal to

$$AR = \frac{L}{R}, \tag{3.15}$$

The cross section moment of inertia (vertical load, coaxial to the beam's longitudinal axis) is:

$$J = \frac{2(\pi R)^4}{64}, \tag{3.16}$$

For the boundary conditions of clamped base and free tip we have:

$$P_{cr} = \frac{\pi^2 E.J}{4L^2}, \tag{3.17}$$

Whereas, for clamped base and clamped tip the critical value is:

$$P_{cr} = \frac{4\pi^2 E.J}{L^2}, \tag{3.18}$$

Where the effective length is:

$$L_{eff} = 2L\,, \tag{3.19}$$

Having the theoretical foundation, it was proceeded to carry out a MATLAB simulation. The figures 3.14, 3.15, and 3.16 display these results. The graphs depict the potential pull-off force simulation with the applied force as the controllable variable and the maximum force that can be applied to the mushroom-shaped pillar taken into account.

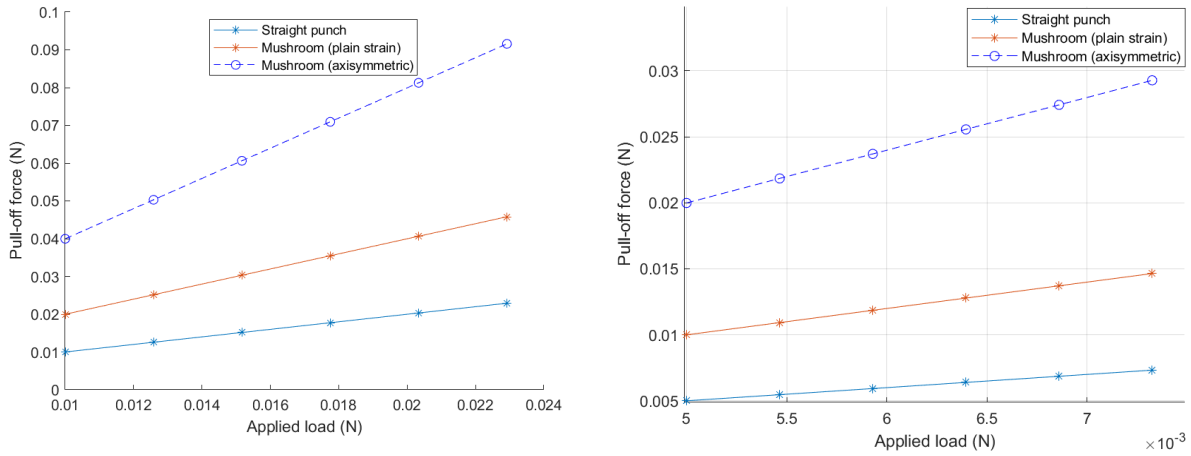

Figure 3.14 – Pull-off force obtained through the applied force when assuming: E=21,77 KPa , D=0,67 mm , D_f=1,33 mm (left); E=21,77 kPa , D=0,50 mm , D_f=1,00 mm (right).

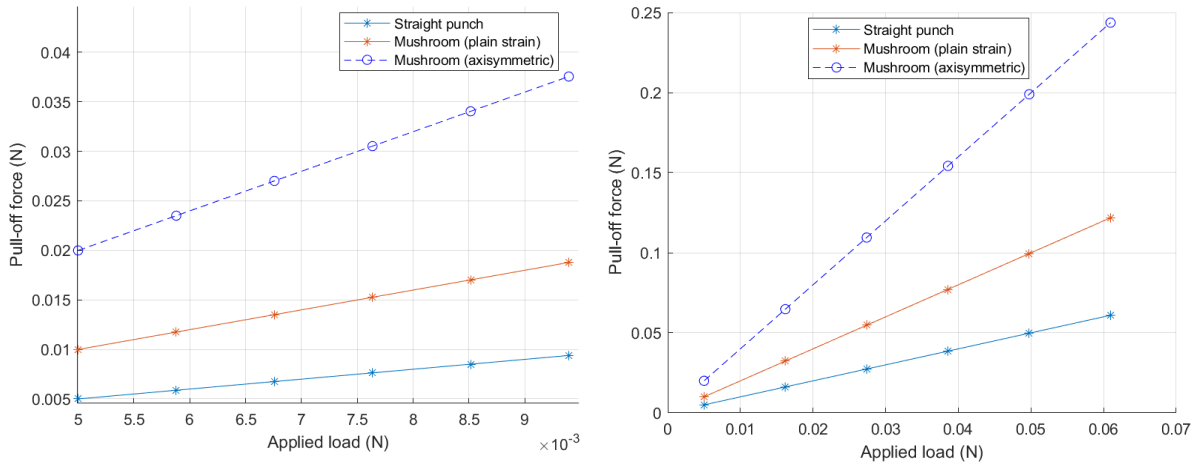

Figure 3.15 – Pull-off force obtained through the applied force when assuming: E=27,92 KPa , D=0,50 mm , D_f=1,00 mm (left); E=21,77 kPa , D=0,67 mm , D_f=1,33 mm (right).

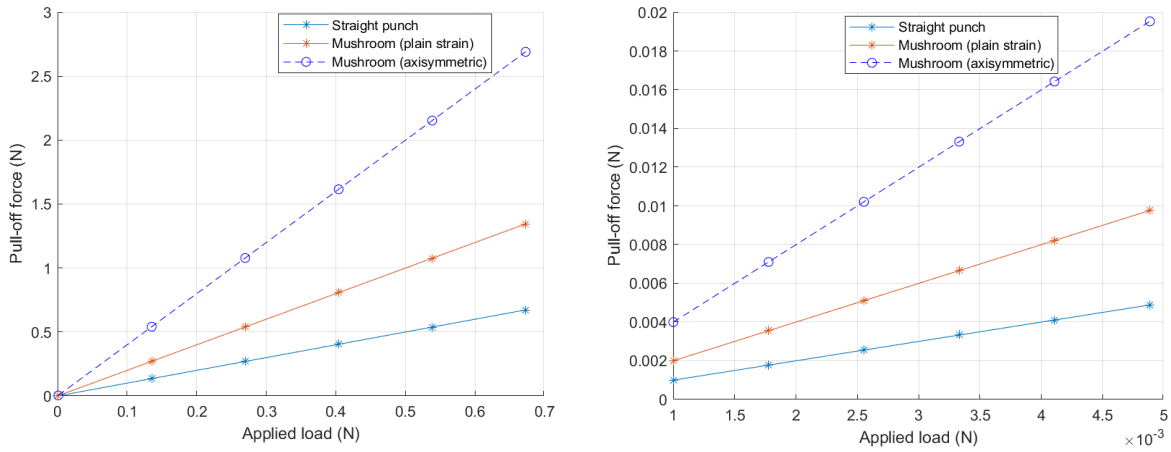

Figure 3.16 – Pull-off force obtained through the applied force when assuming: E=2,00 MPa , D=0,50 mm , D_f=1,00 mm (left); E=14,52 kPa , D=0,50 mm, D_f=1,00 mm (right).

Some of the conclusions that can be drawn from these graphs are that the geometry of the mushroom shaped pillars plays an important role in the bonding mechanism, and that increasing the Young's modulus causes an increase in the pull-off force. This is due to the fact that higher Young's modulus allows to apply higher forces to the material and thus obtain better pull-off forces.

4. FABRICATION OF THE STRUCTURES

In this section are detailed the processes for the fabrication of the mechanical characteristic samples, the manufacture of PDMS mushroom arrays and the manufacture of different MRE structures, with a PDMS matrix and a determined percentage of carbonyl particles.

4.1. MECHANICAL CHARACTERIZATION OF PDMS: SPECIMEN DESIGN AND FABRICATION

With the objective of performing tensile and compressive tests on the Sylgard 184 PDMS in order to look into its mechanical properties, it was designed different negative molds in acrylic. These molds possess a geometry in accordance with the respective American Society for Testing of Materials (ASTM) standards (ASTM D412 standard and ASTM D1229 – 03) for tensile, Figure 4.1, and compressive testing of rubber and elastomeric materials.

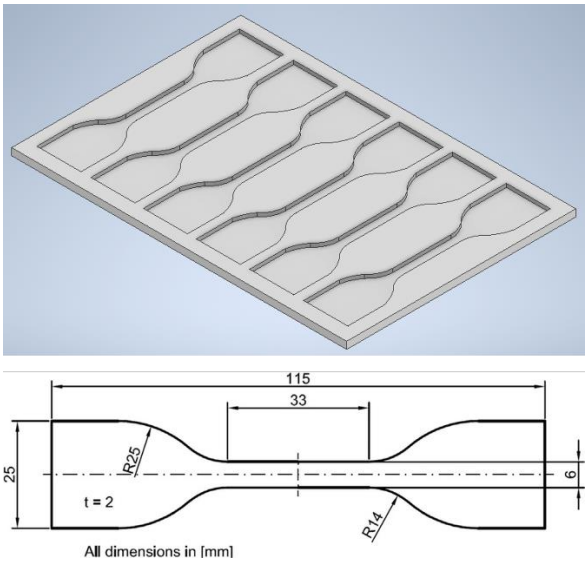

Figure 4.1 – Geometry and dimensions of the tensile specimens in accordance with the American Society for Testing of Materials (ASTM) standards.

Various curing temperatures and PDMS base to curing agent mixing ratios were taken into account during these testing to evaluate their impact on the material's characteristics.

Having designed the mold, the test specimens were manufactured using a laser cutter, and a CNC and cast from a plate of Poly(methyl methacrylate) (PMMA), Figure 4.2.

Figure 4.2 – Tensile (left) and compression (right) negative molds.

The compression molds are cylindrical samples with a diameter of 9 mm and a height of 10 mm, made with a laser cutter. Two parts made up the compression mold. The base is made of a 4 mm thick PMMA plate, while the top section is made of a 10 mm thick PMMA plate. The tensile molds were fabricated using the CNC.

PDMS preparation

The *Sylgard 184* silicone elastomer is supplied as a two-part liquid component kit (a pre-polymer base and a cross-linking curing agent) that when mixed together can be cured at room temperature (approximately 25 °C) or at higher temperatures with lower curing times.

To remove the bubbles of air in the uncured PDMS, this one is thoroughly degassed in a vacuum desiccator at low pressure. Afterwards the degassed PDMS is poured into the molds. The filled molds are then put in the oven for a previously determined time and temperature, these values can be found in Table 4.1.

Table 4.1 – Ratio, time and temperature used in the samples tested

Ratio [w]	Curing Time (hours)	Temperature (°C)
1:10	1	85
	48	25
	4	65
1:5	4	65
1:15	4	65

Lastly, the samples were carefully demolded and are ready to be characterized, Figure 4.3.

Figure 4.3 – Tensile (left) and compression (right) characterization specimens.

In the two part molds, compression, during the demolding of the molds, it was observed that some material migrated from the cavity to the space between the base and the top part, making some the test pieces concave.

After curing, several air bubbles were discovered around the PDMS pieces of 1 mm thickness, particularly in the zone to be tested. Their presence would cause the piece to rupture more easily in that zone during tensile testing, therefore influencing the final results.

4.2. FABRICATION OF INDIVIDUAL PILLARS

In the interest of initial adhesion tests, a few individual pillars were fabricated. The dimensions of these pillars are listed in Table 4.2.

Table 4.2 – Dimensions of pillars fabricated.

[mm]	**1**	**2**	**3**	**4**	**5**	**6**	**7**	**8**
Radius	0,5	0,5	0,5	0,5	1	1	1	1
Hight	0,5	1	1,5	2	1	2	3	4
Aspect Ratio	1	2	3	4	1	2	3	4

The negative mold was molded in *Inventor CAD* and fabricated using the milling machine CNC *FlexiCam Viper* (Figure 4.4).

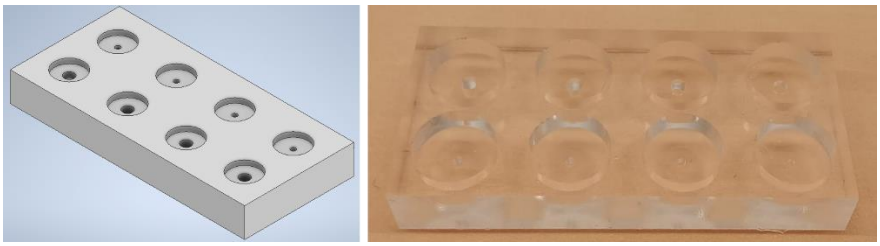

Figure 4.4 – Negative mold in Inventor CAD (left). Mold obtained from CNC (right). Each pillar negative exhibits different sizes.

PDMS Sylgard is mixed with curing agent in 10:1 w/w in a plastic cup and then degassed in a desiccator for 20 minutes. Afterward, this liquid PDMS is poured onto the negative mould. Later on, the structure is degassed under vacuum for 45 minutes in order to remove air trapped then cured at 65°C for 4 hours.

4.3. MICROSTRUCTURES FABRICATION

The objective of this fabrication is to obtain an adhesion mechanism prototype with the subsequent intention of analyzing the adhesion properties present

For this fabrication it is being followed the protocol presented in the chapter 2.4.4. Double molding.

The fabrication of the microstructures consists of three main processes. These include printing the resin structures (that will act as positive molds), creating the Ecoflex negative mold, and finally fabricating the PDMS structure. In the next chapters (4.3.1, 4.3.2, 4.3.3) the mention steps are addressed in more detail.

In Figure 4.5, the workflow of the protocol being followed for the fabrication of microstructures is showed.

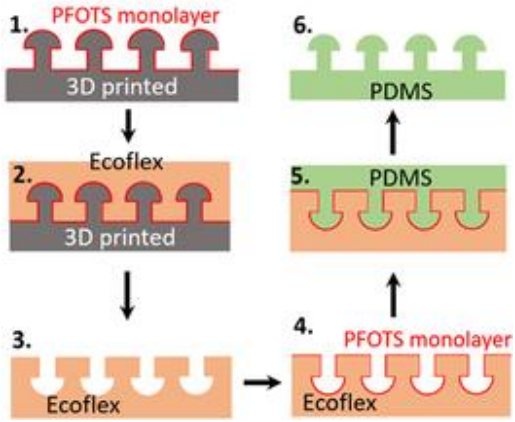

Figure 4.5 – Schematic illustration of double molding procedure; 1. 3D printed mold 2. molding Ecoflex on 3D printed, 3. negative mold in Ecoflex 4. monolayer deposition of perfluorodecyltrichlorosilane (PFOTS) by chemical vapor deposition 5. casting PDMS in Ecoflex mold and 6. PDMS sample (Sharma et al., 2021a).

4.3.1. Fabrication of positive mold

The positive molds in this process are fabricated in the SLA 3D printer using grey resin. First of all, in order to modulate the structures for printing, the software *Inventor Cad* was utilized.

Then, to produce the polymeric structures, it was utilized the 3D Printer SLA - Formlabs Form2.

Lastly, these microstructures can be silanized or not depending on the necessity of an easier demolding. The silanized molds are considerably easier to demold then the not silanized ones. The silanization procedure is explained in the next subchapters.

In Figure 4.6 shows one example of a positive mold that is used to create the negative mold on Ecoflex, which in turn is used to obtain the PDMS structures.

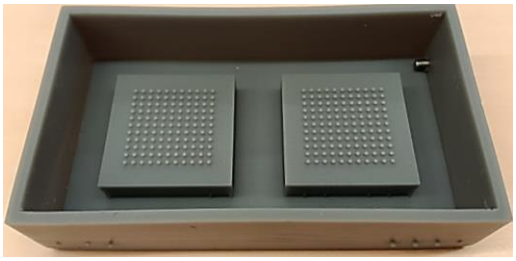

Figure 4.6 – Printed mold in 3D printer SLA.

4.3.2. FABRICATION OF NEGATIVE MOLD

Once the resin microstructures (positive molds) are ready, the next step is to produce the negative mold. For the manufacture of this will be used the silicone Ecoflex 00-30. The main reasons of the use of this material as a negative mold is because it's a very soft and very strong rubber that can stretch many times its size without break, fact essential during demolding.

Ecoflex 00-30 part A and part B were mixed together in a ratio 50:50 w/w for 10 minutes and left under vacuum for 5 minutes for removing the air trapped in the viscous liquid. After that, the Ecoflex was poured on top of the 3D printed structure and it was degassed again under vacuum for, approximately, 30 minutes, Figure 4.7.

Figure 4.7 – Degassing of air in a vacuum desiccator.

Then the Ecoflex is cured the at room temperature for 2 h and post cured at 65°C in an oven for another two hours (Sharma et al., 2021b). Being cured, the Ecoflex is peel off (gently) the 3D printed structure using ethanol as a lubricant between the two surfaces. The negative mold (Figure 4.8) is cleaned with ethanol or IPA and dried.

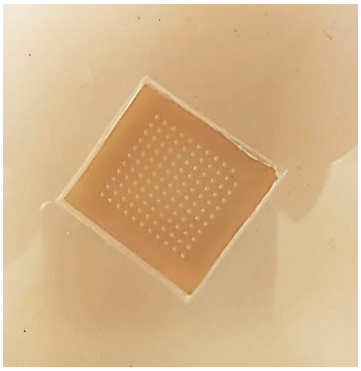

Figure 4.8 – Negative mold, in Ecoflex, demoulded and cleaned, ready to go under the PFOTS coating.

Afterwards, in order to facilitate demolding, the silanization, also called the PFOTS coating, is performed.

The first step in the PFOTS coating procedure (silanization) is submitting the samples to an oxygen plasma treatment. To perform the plasma activation was used the *Plasma Cleaner PDC-002.*

The air and oxygen plasma were both experimented, however better results were obtained when using the oxygen. This could be to the fact that when using air plasma there are several gases in the plasma gas (air) that influence the process. On the other hand, the oxygen plasma only has one gas (oxygen) making it more concentrated.

After several experiments the plasma cleaner parameters that showed better results were using the oxygen plasma at high power, at a pressure of, approximately, of 350 mTorr, for 30 seconds.

Then the mold is put into a desiccator along with 0,2 milliliters of the silane. The silane is put on aluminium foil. Then the vacuum is turned on. Having the dissector under vacuum, with the intent of helping the silane vaporization, it's put the desiccator, in the oven at 65 degrees Celsius overnight, Figure 4.9.

Figure 4.9 – The picture in the left is inside the fume hood where the silanization is prepared. In the right picture the desiccator is in the oven, where it stays overnight at a temperature of 65°C.

To finalize the coating procedure the samples are removed from the desiccator and are to be left in an oven at 65°C for an hour. Then, they are washed with IPA (isopropanol) after this the structures can be used for the fabrication of the PDMS structures.

During the course of this work there was a need to change/test several variables. For example, initially the silanization was performed without temperature control however this process did not work in the Ecoflex molds. Even though, throughout this initial process the resin microstructures were successfully silanized, the process resulted in the bonding between the Ecoflex and PDMS.

In Figure 4.10, it can be noticed the bonding that happens between PDMS and Ecoflex when it is not performed the silanization on the negative mold or when this one is not successful.

Figure 4.10 – Ecoflex bonded with PDMS. On the left, the sample was not subjected to silanization. On the right image, the sample was subjected to an initial silanization process.

The Ecoflex molds need to be silanized, contrary to the resin microstructures. If the resin microstructures are not silanized a favorable demolding can still be achieved, it will not be as

easy as if the structures are silanized, but their demolding is still attained. The same it is not true for the Ecoflex molds.

4.3.3. FABRICATION OF PDMS MICROSTRUCTURES

To start the fabrication of PDMS microstructures it is mixed the PDMS *Sylgard 184* with the curing agent (in a ratio 10:1) and then degassed in a desiccator.

The resultant mixture is poured onto the Ecoflex negative mold (that has been treated with PFOTS). After, the structure is, again, degassed under vacuum in order to remove all air bubbles trapped in the microscopic asperities within Ecoflex, this process takes about an hour. Then the structure is cured at 65°C in an oven for 4 hours.

Finally, the cured PDMS microstructure (Figure 4.11) is peeled off, very carefully, from the Ecoflex using IPA (isopropanol) as a lubricant between the two surfaces.

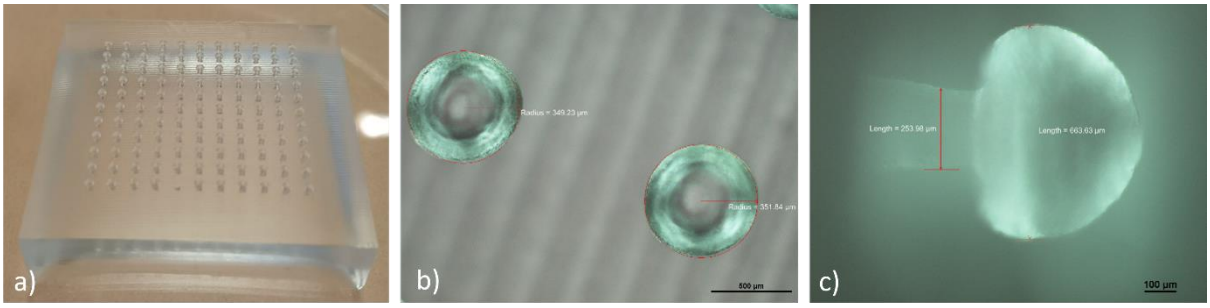

Figure 4.11 – Images of PDMS microstructure. a) PDMS microstructure resulting from the double molding process; b) optical microscopy from the top; c) side microscopy image.

Numerous trials involving a variety of factors were carried out before the current methodology for the manufacture of microstructures was established. Since each of the micropillars in some structures were broken unevenly.

In one of these tests, to make the Ecoflex softer and easier to demould, the Ecoflex molds were adjusted by reducing the thickness in the area of the micropillars.

In several tests, the issue was that different percentages of the mushroom shaped micropillars were complete while the others broke when demolding (Figure 4.12). This occurrence could be due to the fact that the dispersion of the silane in the Ecoflex mold is not homogeneous, as this factor cannot be controlled using the vaporization silanization method, or it could be due to the demolding process.

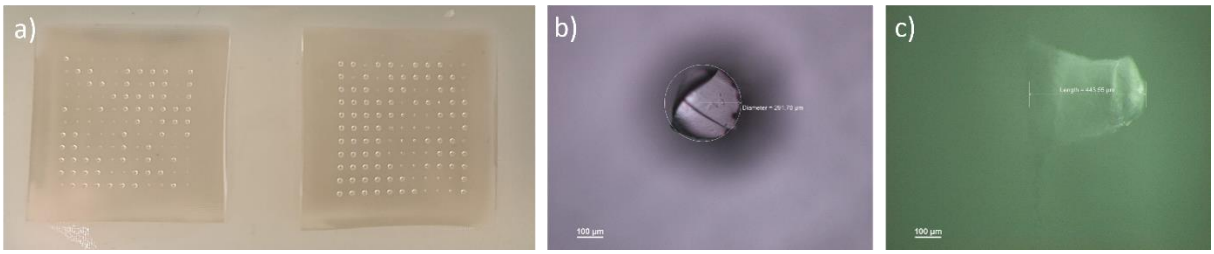

Figure 4.12 – PDMS microstructures. a) Various percentages of broken pillars in samples; b) top and (c) side optical microscopy images.

With the intention of obtaining a more homogeneous signalization, it was opted to perform an immersion silanization. To do this, it was made a solution of ethanol in which was dissolved 1% of silane, and this solution was poured into the negative mold overnight. However, this solution did not improve the silanization process.

Different curing conditions were tested in order to decrease the curing time. This test is important for curing the MRE samples, because the curing conditions are 1 hour at 85 degrees Celsius.

It was also tested if it was possible to reuse the Ecoflex molds. However, this did not work. Some pillars were intact but most broke during demolding, Figure 4.13.

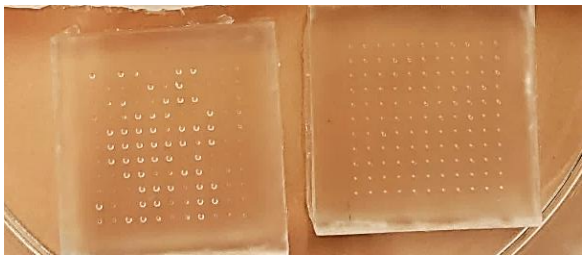

Figure 4.13 – Resulting PDMS structure fabricated reusing an Ecoflex mold. All the micropillars in the sample to the right broke during the demolding procedure.

One inference that may be drawn from this test is that the silane coating that was previously present on the Ecoflex may have transferred to the PDMS pillars.

4.4. Fabrication process of the adhesion mechanism prototype

Essentially, creating an MRE involves mixing the basic ingredients (PDMS, additives, and particles), then curing to embed the particles in the polymeric matrix. Multiple MREs were

built throughout this project as problems arose and solutions were discovered, and the production process was enhanced.

No additives were added to the matrix; instead, only PDMS and carbonyl iron particulates were used to create the MREs in this study.

The process is divided into several steps, starting with mixing the PDMS, in a 10:1 ratio between the base and the curing agent, with the particles. According to the mass of the PDMS (base + curing agent), the mass concentrations of 40% and 80% were taken into consideration to explore the impact that particle concentration can have on the MRE's microstructures characteristics.

Mixing Procedure

The PDMS base and curing agent are mixed together before to adding the particles and resuming the mixing operation (Pereira, 2022).

The procedure begins with the weighting of each component in accordance with the mass required for the respective molds, followed by the mixing of the PDMS base and curing agent for 15 minutes at 2000 rpm in an IKA Eurostar 200 mechanical stirrer, followed by the addition of the particles and mixing for an additional 15 minutes at the same speed (Pereira, 2022), Figure 4.14.

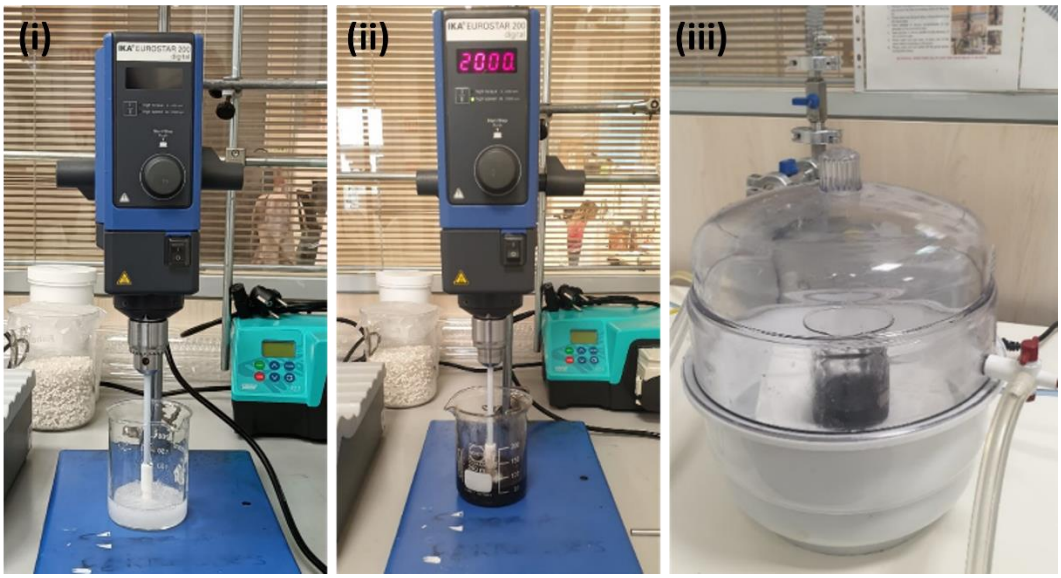

Figure 4.14 – Mixing of the PDMS (i) and the MRE (ii) components on a mechanical stirrer *IKA Eurostar 200;* degassing of the MRE mixture in a vacuum desiccator (iii).

After this process, the mixture is completely degassed in a vacuum desiccator, Figure 4.14. Subsequently, the polymeric mixture is poured onto a mold and put back in the desiccator until there are no air bubbles left. Once degassed, the mold is placed in the oven. The curing parameters are one hour at 85 degrees Celsius.

Once the samples are cured, the procedure of demoulding is carried out, achieving the desired structures, as it shows in Figure 4.15.

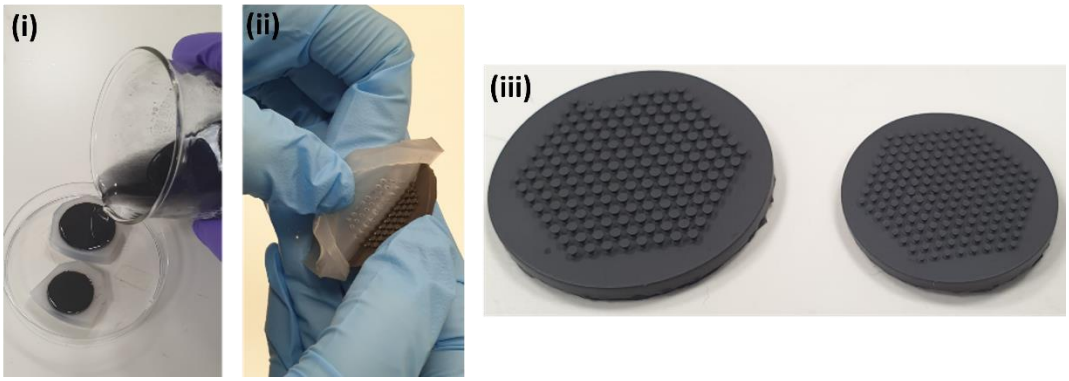

Figure 4.15 – The image (i) shows the poring of MRE mixing in the mold, the image (ii) shows the demolding process, and the image (iii) shows the obtained microstructures.

The results obtained from this process were favourable. It was expected that the introduction of the nanoparticles would result in the intrusion of more stress in the structure and that the pillars would break more easily, however, none of them did.

5. RESULTS AND DISCUSSION

In this section are described the experiments performed to evaluate the 3D printer capability of producing the necessary microstructures and to evaluate the mechanical properties of PDMS as well as the adhesion mechanism on pure PDMS and the MRE system.

5.1. EVALUATING 3D PRINTING'S FABRICATION

Given that in this study, in order to fabricate the molds for the fibrils array, it is being used an SLA 3D printer, and knowing from research that for a better adhesion are recommended dimensions in micro and nano scale. Towards the purpose of evaluating the capability of the SLA 3D printer of producing the necessary microstructures it was printed several arrays containing mushroom shapes fibrils of different sizes, considering several ratios between the dimensions, and the 3D printer resolution (Figure 5.1).

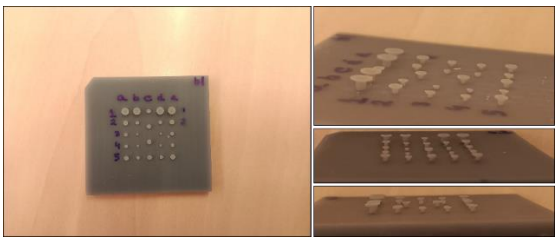

Figure 5.1 – Mushroom-shaped structures fibrils of diverse dimensions.

In Table 5.1, the dimensions used for these mushroom-shaped structures are described.

Table 5.1 – Dimensions, in mm, used for the Figure 5.1 mushroom-shaped structures.

Height of cap	Diameter of cap	Diameter of stalk	Height of stalk
0,1000	0,6000	0,3000	0,6000
0,1000	1,2000	0,6000	1,2000
0,1000	0,6000	0,3000	0,6000
0,1000	1,2000	0,6000	1,2000
0,2000	1,2000	0,6000	1,2000
0,2000	0,6000	0,3000	0,6000
0,2000	1,2000	0,6000	1,2000

0,1000	0,6667	0,3333	0,6667
0,1000	1,0000	0,5000	1,0000
0,1000	2,0000	1,0000	2,0000
0,1000	0,6667	0,3333	0,6667
0,1000	1,0000	0,5000	1,0000
0,2000	0,6667	0,3333	0,6667
0,2000	1,0000	0,5000	1,0000
0,2000	2,0000	1,0000	2,0000
0,2000	0,6667	0,3333	0,6667
0,2000	1,0000	0,5000	1,0000
0,1000	1,0000	0,5000	1,0000
0,1000	1,3333	0,6667	1,3333
0,1000	2,0000	1,0000	2,0000
0,1000	1,0000	0,5000	1,0000
0,1000	1,3333	0,6667	1,3333
0,2000	1,0000	0,5000	1,0000
0,2000	1,3333	0,6667	1,3333
0,2000	2,0000	1,0000	2,0000
0,2000	1,0000	0,5000	1,0000
0,2000	1,3333	0,6667	1,3333

Subsequently, the previous microstructures were subjected to the previously described double molding process in order to evaluate the resulting mushroom shaped PDMS pillars.

Some of these microstructures were chosen for positive molds (Figure 5.2) after they had been analysed.

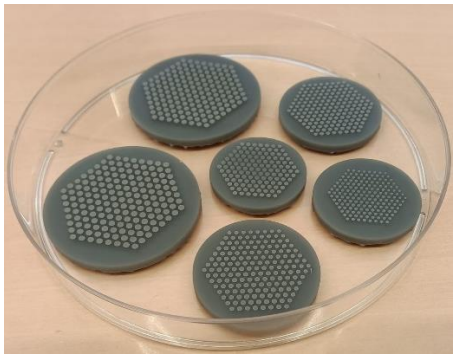

Figure 5.2 – Microstructures obtain by the SLA 3D Printer.

The arrays of mushroom-shaped pillars in Figure 5.2 are in a hexagonal pattern in order to obtain the same distance between each. These structures serve as positive molds in the manufacturing process.

Having printed several microstructures, these were used as a positive mold, from which (applying the double molding method described above) PDMS microstructures were obtained.

The PDMS microstructures were inspected with access to an optical microscope, Figure 5.3.

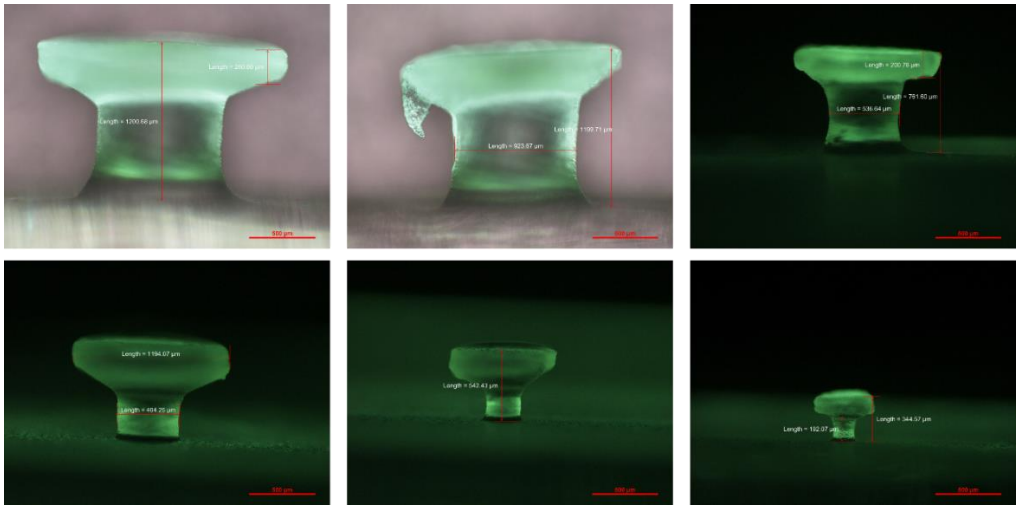

Figure 5.3 – Images obtained in the optical microscope Eclipse L200N, showing some of the micropillars manufactured.

With these results, it was proceeded to the selection of some dimensions of mushroom shaped pillars in order to obtain an array of these pillars to evaluate their adhesion.

5.2. CHARACTERIZATION OF THE PDMS

To the characterization of the PDMS, the specimens were put through a tensile test on a Universal Testing Machine SHIMADZU in accordance with the ASTM D412 and the ASTM D1229-03 standards (Thackeray, 2022). A guideline used for assessing the tensile and compressive characteristics of thermoplastic elastomers and vulcanized rubber.

The stress-strain curves for the tensile testing of each pure PDMS sample were acquired, allowing one to see how the curing temperature affects the material's mechanical characteristics, particularly the Young's modulus.

The stress-strain curves for each PDMS sample at curing temperatures of 65°C, 85°C and "room temperature" are shown in figures 5.4, 5.5 and 5.6.

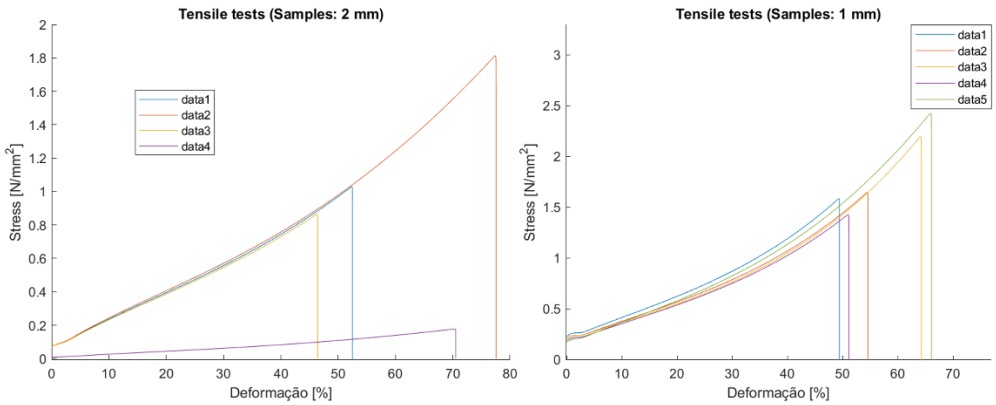

Figure 5.4 – Tensile stress-strain curve for tensile tests carried out on PDMS samples that had been cured at 65°C with a 10:1 mix ratio.

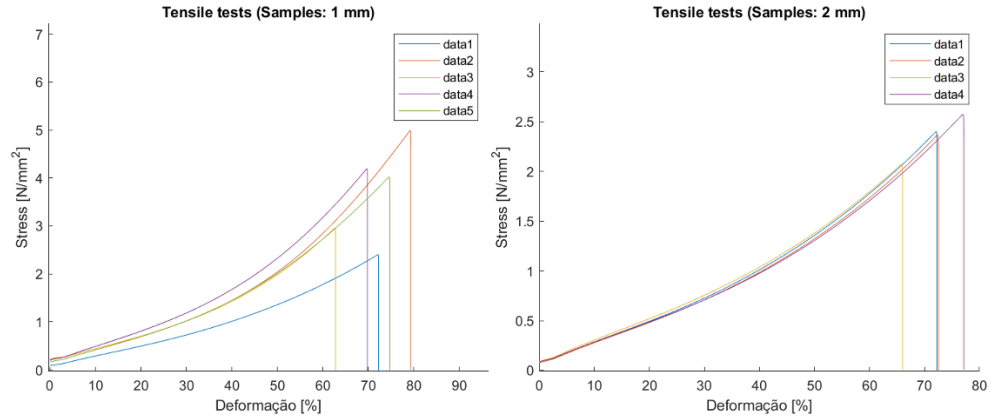

Figure 5.5 – Tensile stress-strain curve for tensile tests carried out on PDMS samples that had been cured at 85°C with a 10:1 mix ratio.

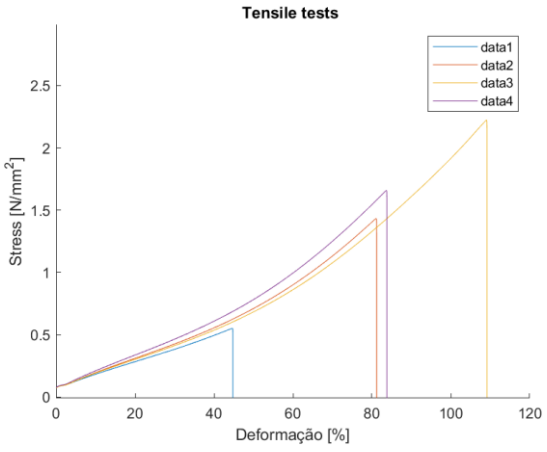

Figure 5.6 – Tensile stress-strain curve for tensile tests carried out on PDMS samples that had been cured at room temperature with a 10:1 mix ratio.

Some graphs present less samples than other due to the fact that some samples fractured or had defects due to trapped air bubbles, that weren't extracted during degasification.

The Young's modulus of the PDMS samples was determined for the linear elastic region (up to 40% strain), and the results are shown in Table 5.2.

Table 5.2 – Young's modulus obtained from the tensile tests.

Curing Temperature (°C)	Young's Modulus (MPa)
25	0,012
65	0,017
85	0,023

The findings indicate that the Young's modulus increases as the PDMS's curing temperature does. The values obtained appear to be lower than the results for Young's modulus that are often seen in publications, which range from approximately 100 kPa to 10 MPa (Balijepalli et al., 2016).

The Young's modulus obtained in the compressive tests for the PDMS samples cured at 85°C was 0,019 MPa.

5.3. EXPERIMENTAL VALIDATION OF ADHESION MECHANISM

Usually experiments investigating the adhesion of these patterned surfaces press flexible fibrils against a stiff spherical substrate or a flat surface with predefined roughness and the adhesive strength is then evaluated during subsequent tensile loading.

5.3.1. ADHESION EXPERIMENTS ON INDIVIDUAL PILLARS

It was employed the UTM to perform the experimental tests, on the individual pillars previously fabricated.

Figure 5.7 depicts a typical force-displacement curve for a standard pull-off experiment employing a spherical probe. The pull-off force is calculated as the highest tensile force

measured after a given compressive preload has been applied. The work of adhesion is related to the area covered by the force-displacement curve.

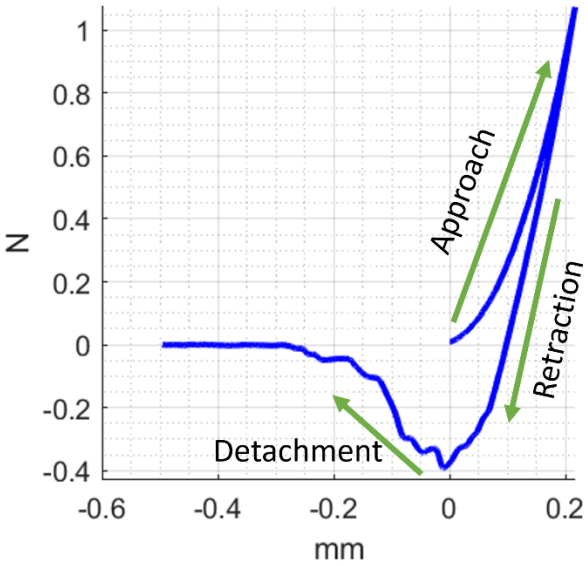

Figure 5.7 – Force displacement curve for a normal adhesion test. Sample approaches the probe, contact is formed, and the soft sample is compressed with a defined preload, and then retracted until detachment occurs at a certain pull-off force. The maximum of the tensile force is defined as the pull-off force. Note that tensile forces are designated as negative, compressive forces as positive.

In Figure 5.8 are several plots each one corresponding to a different pillar. These pillars were made of PDMS and the dimensions for each pillar are listed in Table 4.2.

Given that tensile forces are designated as negative and compressive forces as positive, the maximum tensile force that is obtained is the pull-off force necessary to detach the pillar from the compression plate.

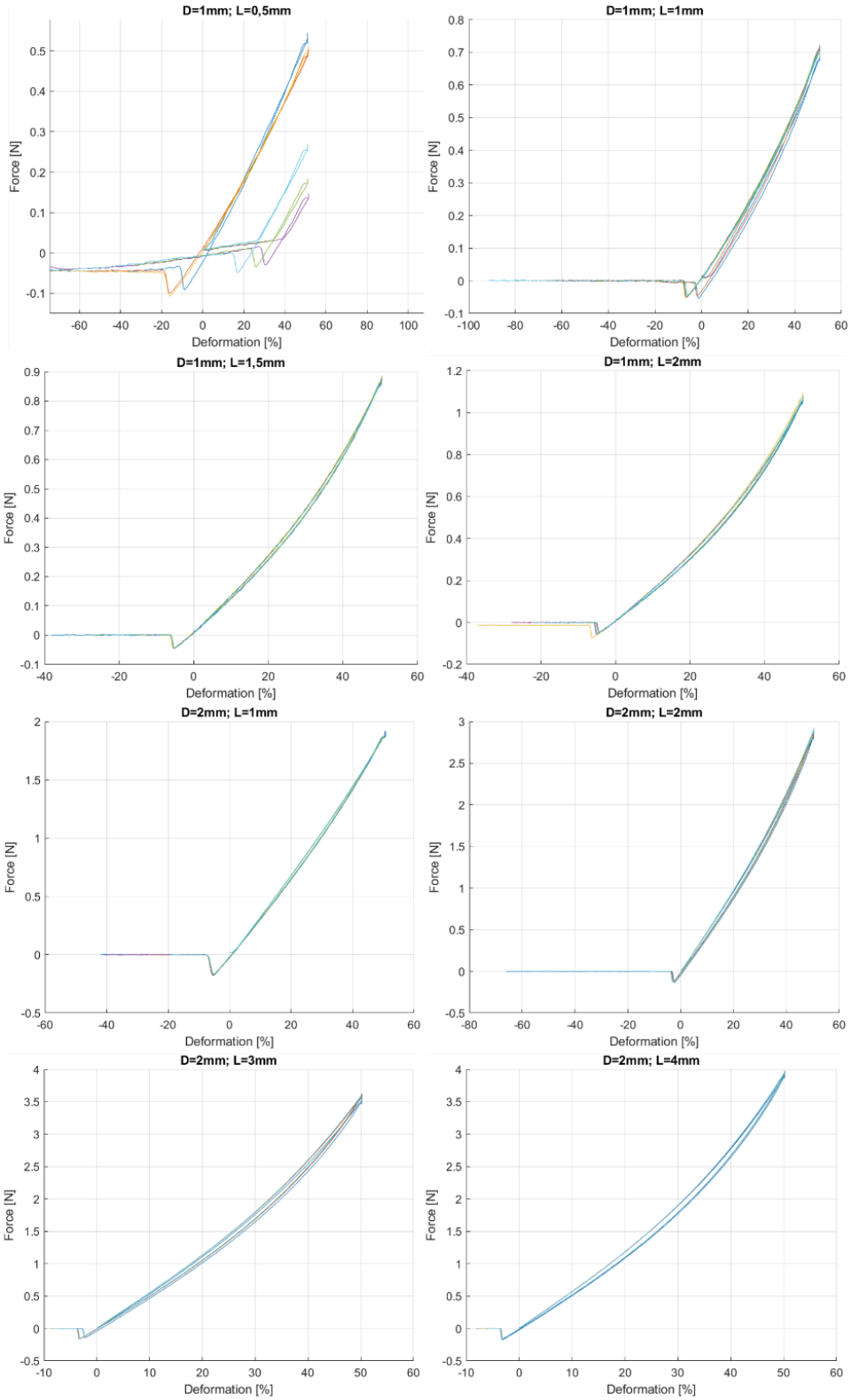

Figure 5.8 – Each plot shows a force deformation curve relative to the data collected from normal adhesion experiments carried out on 8 distinct PDMS pillars. Each plot title includes a description of their dimensions (their diameter (D) and length (L)).

Analysing the graphs (Figure 5.8), it appears that the pull-off force generally increases as the applied force increases. Although it cannot be confidently said that this rise is caused

by any specific aspect, given that the pillars all have different dimensions The D=2 mm; L=1 mm pillar, which was the shortest of the four with a diameter of 2 mm was the one that consistently produced superior results.

Figure 5.9, is an expansion of four plots from Figure 5.8 so that it can be seen the pull-off forces better. As can be shown, aspect ratios have no impact on the pull-off forces.

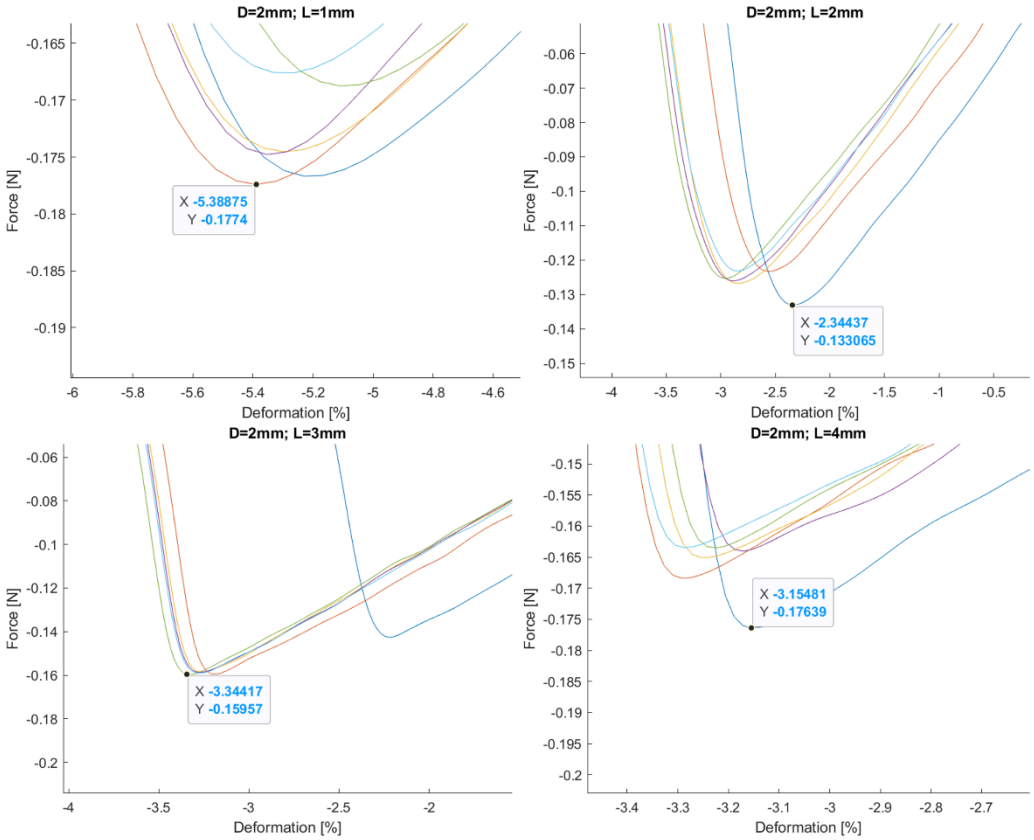

Figure 5.9 – Expansion of four plots presented in Figure 5.8. These plots correspond to those that correspond to pillars with a diameter of 2 mm and an aspect ratio of 1, 2, 3 and 4.

With the posterior manufacture of microstructures with the addition of microparticles in mind, structures with the same geometry but composed of a magnetorheological elastomer (MRE) were created. This elastomer was fabricated by adding to a PDMS matrix 40% and 80% amounts of carbonyl iron particles (CIP).

Afterwards, the previous tests were repeated on all samples under the same conditions. In these tests a force of 1.23N was applied, followed by its retraction and the force required to detach the compression plate from the sample was recorded. The results of these tests are shown in the plots of the Figure 5.11. Each bar in these figures represents the average of the

maximum values of tensile force (pull-off force) that could be measured during adhesion tests to each column.

Published data for the influence of the aspect ratio on the adhesion of patterned surfaces is contradictory. However, it is generally theorized that a high aspect ratio can result in higher adhesion strength (Y. Wang et al., 2014). When applying the same force (1,23 N) to the all the pillars (Figure 5.10 (a)) and comparing the ones with aspect ratios of 1 and 4 and a diameter of 2 mm it can be observed that the ratio of 1 shows a better performance (superior pull-off force). This occurrence is the opposite of what was expected.

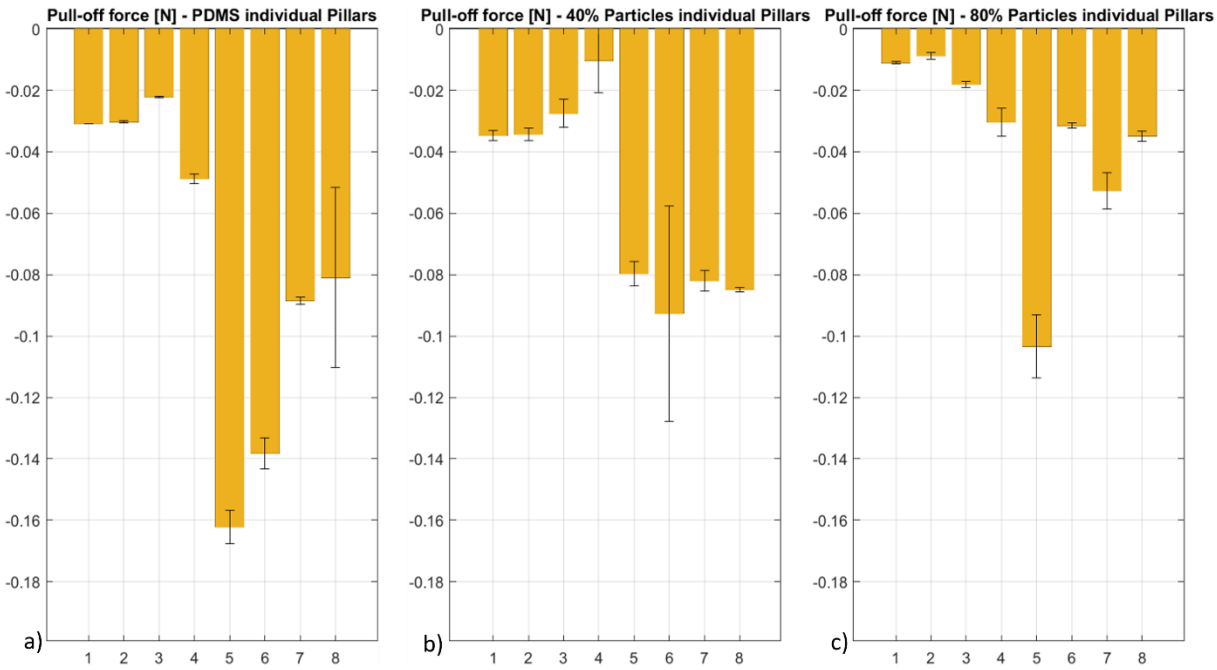

Figure 5.11 – Analysed data of the tested structures. Each column represents the average pull-off forces measured during adhesion tests to PDMS pillars (a), to MRE pillars with 40% of CIP (b), and to MRE pillars with 80% of CIP (c). Each column corresponds to a different pillar listed in Table 4.2.

From the plots in Figure 5.11, it can also be seen that, in general, the PDMS individual pillars show the best performance, followed by the 40% of carbonyl iron particle pillars. Pillars containing 80% of carbonyl iron particles show the worst performance, with the exception of two samples in comparison with those containing 40% of carbonyl iron particles.

It can also be concluded that a larger contact area translates into a better adhesion, since the pillars with a radius of 1 mm systematically show higher pull-off force values.

Higher forces were applied to the pillars during adhesion tests in order to assess the impact that these forces would have on them. The pillars, however, displayed instability (Figure 5.12) and the testes were not continued.

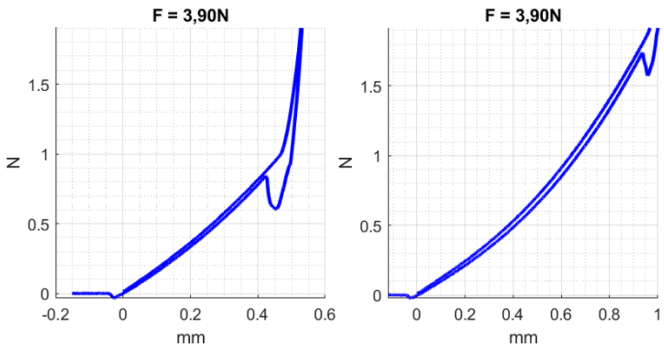

Figure 5.12 – Force displacement curves plotted relative to normal adhesion tests with an applied force of 3,90 N on pillars with diameters of 1 mm and aspect ratios of 1 (right) and 2 (left).

5.3.2. EXPERIMENTAL ANALYSES ON MUSHROOM SHAPED MICROSTRUCTURE

in the current subsection the experimental analyses on mushroom shaped microstructures are presented. The PDMS microstructures fabricated and subsequently analyzed are in Figure 5.13. The surfaces of these mushroom shaped microstructures are hexagonally patterned, so that each micropillar is equally spaced apart.

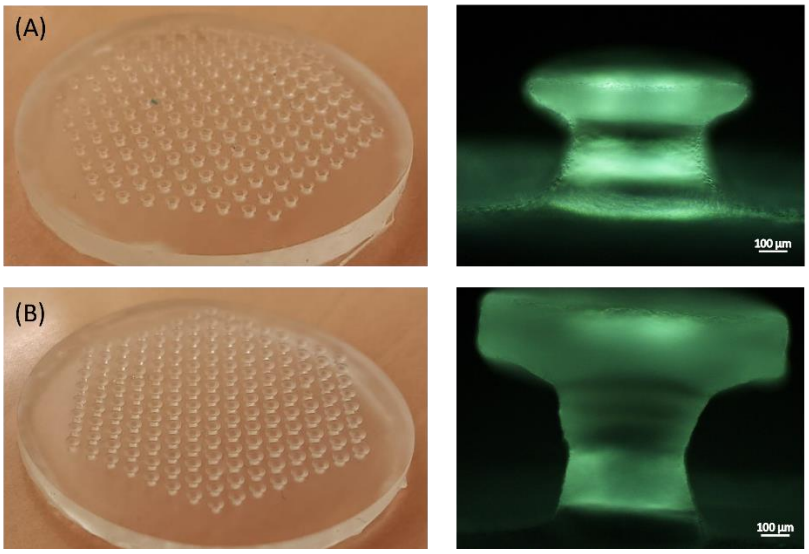

Figure 5.13 – Microstructures used to perform the adhesion experiments.

In the next adhesion tests of Figure 5.14, the same parameters as for the normal adhesion tests applied to the individual pillars were used.

The adhesion performances of the hexagonal patterned surfaces were analyzed by plotting the load-deformation curves obtained. In Figure 5.14, there are two graphs corresponding to these adhesion experiments.

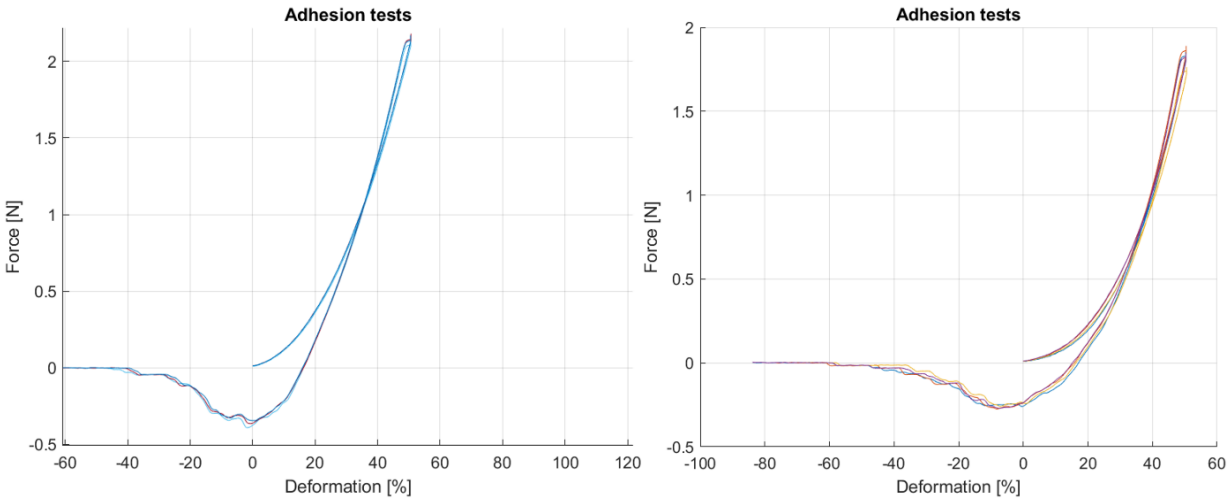

Figure 5.14 – The graph on the left corresponds to the tests performed on microstructures A (left) and B (right). Each plot shows a force deformation curve relative to the data collected from adhesion experiments carried out.

In Figure 5.14 it can be observed that the structure with a better performance (higher pull-off force) was the first one however this one had a higher applied force, given that the variable being controlled was the deformation. So new tests were necessary controlling the force. The suaveness of the curves of the plots from Figure 5.9 cannot be observed in these last, this is due to the array of pillars and the fact that they detach at different moments, creating this irregular curves.

In order to evaluate the influence of the applied force on the pull-off force, new tests were made always applying the same force to a couple of microstructures and individual pillars.

In Figure 5.15, the difference between the curves relative to the adhesion tests performed on microstructures composed of PDMS and MRE can be observed. To the naked eye, the MRE samples do not show adhesion force.

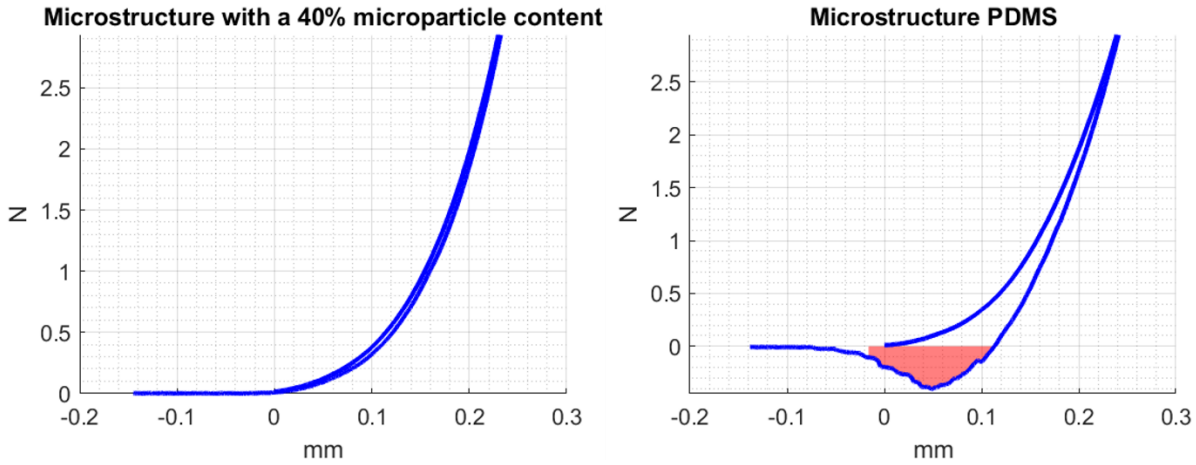

Figure 5.15 – Plots from tests on a microstructure containing 40% CIP versus a microstructure made exclusively of PDMS.

Different forces, 1.23N, 3.90N and 6N, were applied to various microstructures. The data obtained are displayed in Figure 5.16.

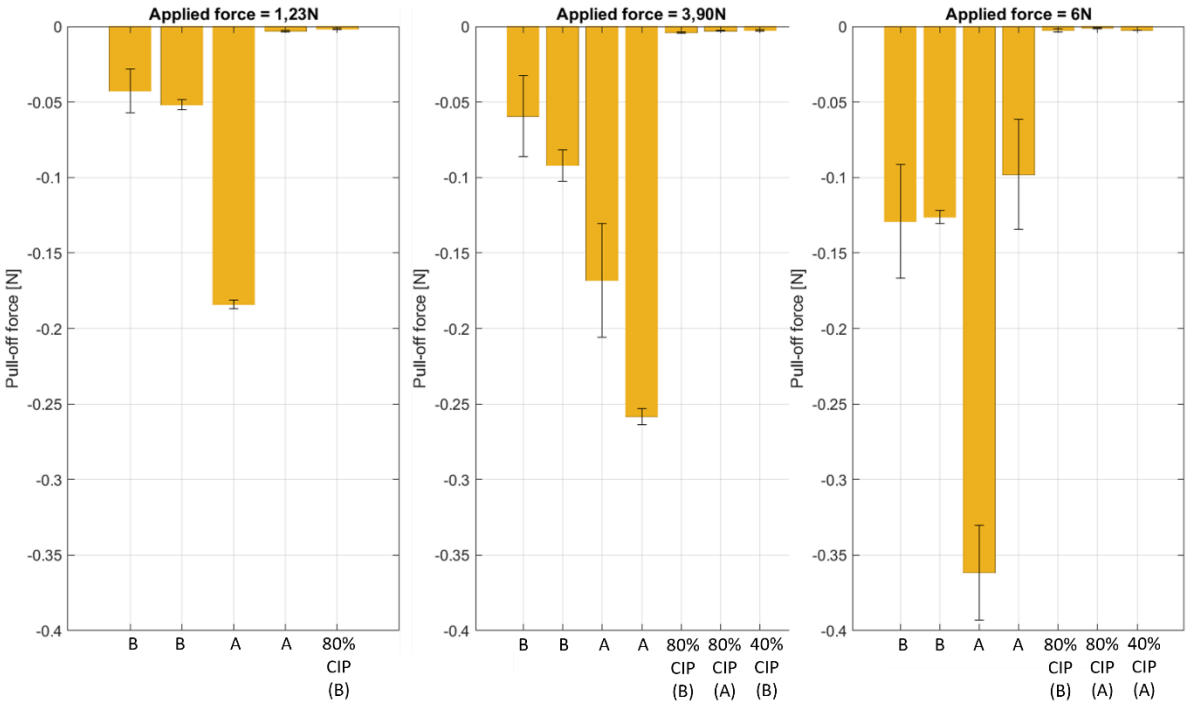

Figure 5.16 – Analysed data of the tested microstructures displaying the average pull-off force measured during adhesion experiments. In the plots, the bars A and B correspond to PDMS microstructures A and B (each with two different samples) from Figure 5.12; the other bars correspond to a microstructure with the same dimensions as A or B but with 80% or 40% of CIP content.

It can be concluded that the results of the microstructures with a CIP content are substantially inferior to the results of the microstructures with only PDMS.

The graphs in Figure 5.17 show only the data obtained for microstructures with integrated CIP. Analysing these plots, it appears that the microstructure with CIP with the same geometry as sample A shows a lower pull-off force than the corresponding microstructure with geometry B. This is the opposite of what happens in a sample with only PDMS, where geometry A shows higher pull-off force values.

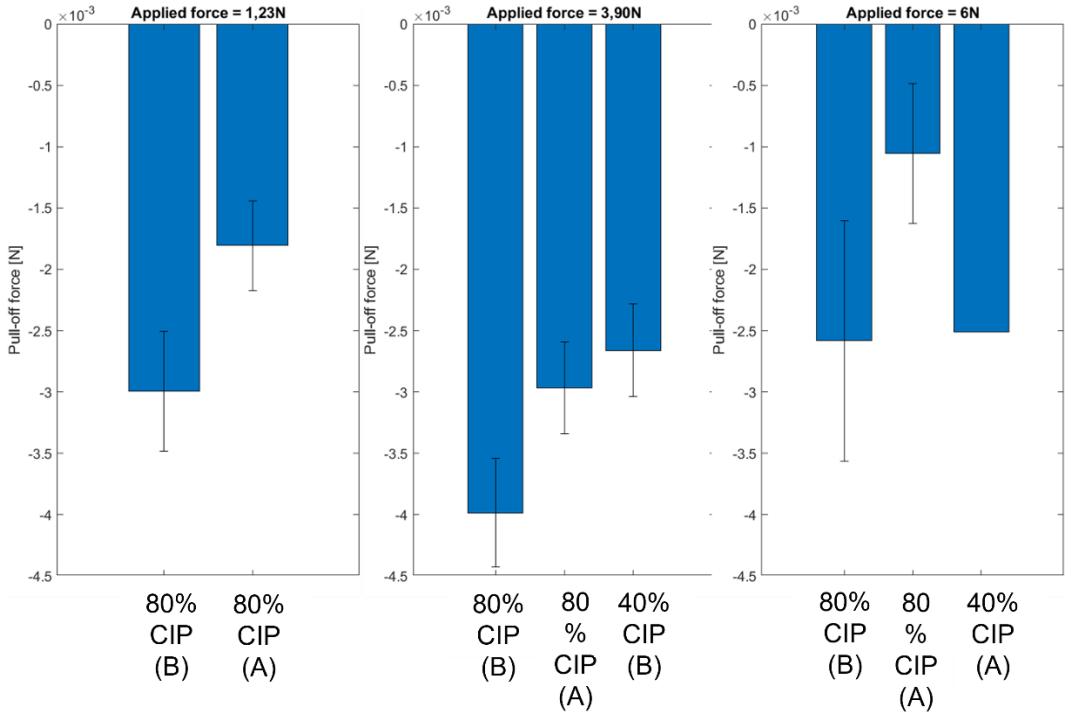

Figure 5.17 – Expansion of plots presented in Figure 5.15 of MRE microstructures' average pull-off force. The bars in the plots represent a microstructure with the same dimensions as microstructures A or B (from Figure 5.12) but containing 80% or 40% CIP.

The expectation would be that the microstructures with CIP would have a better performance due to the fact that with CIP the Young modulus would increase and therefor the pull-off force would also increase. However, an extremely important contributing factor is the roughness and the structures with CIP show a higher rough appearance, Figure 5.18. This factor may account for the results obtained.

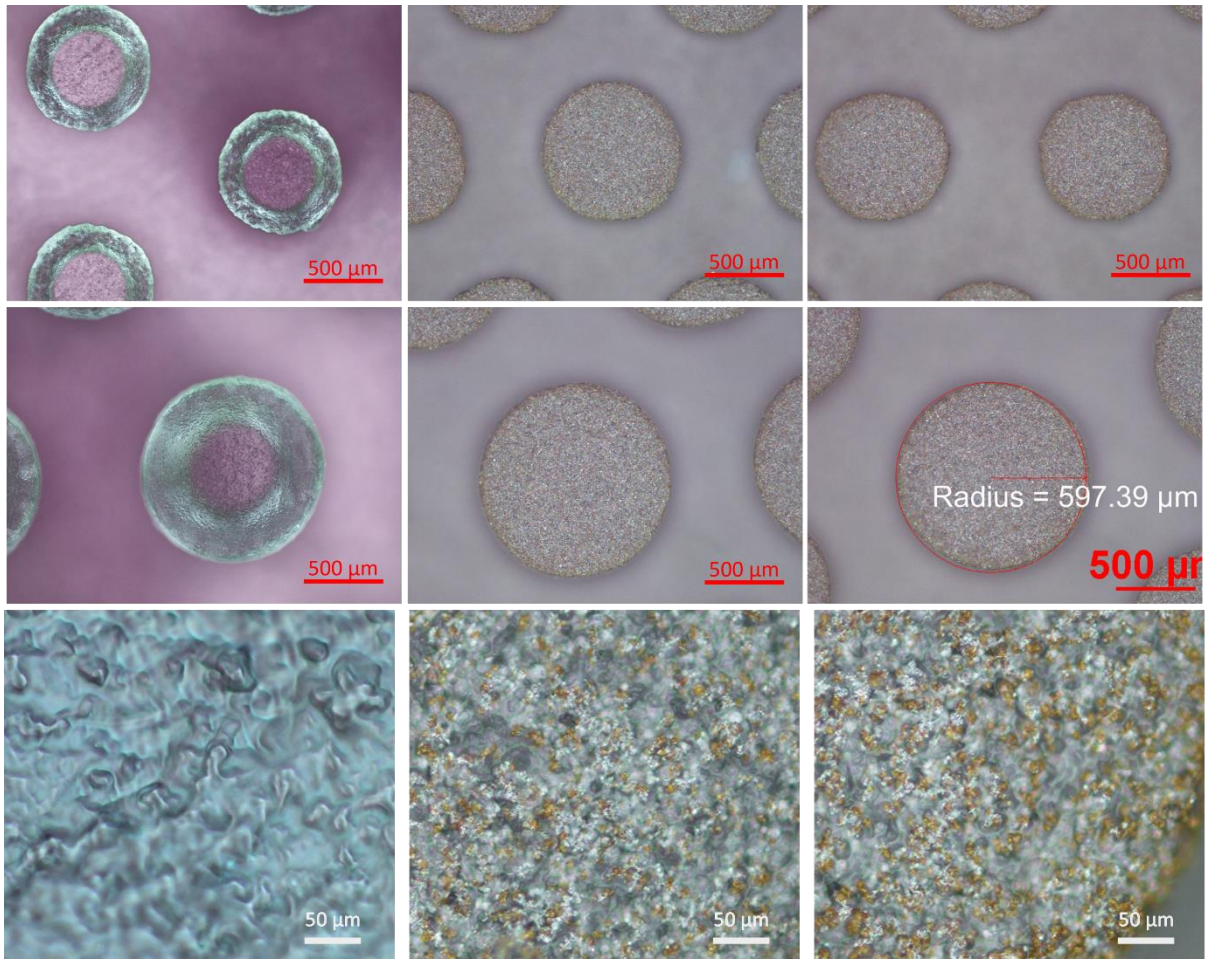

Figure 5.18 – Images obtained in the optical microscope. The images on the left represent PDMS-only microstructures, the images in the middle exhibit microstructures with a CIP percentage of 40%, and the images on the right exhibit microstructures with a CIP percentage of 80%. The images at the top correspond to the microstructure with geometry A, the images in the middle to the microstructure B, and the images at the bottom to the mushroom surface.

Relatively to the MRE mushroom shaped microstructures, their results showed an adhesion that can be consider null. The results can be due to the percentage of particles in the tip, that consequently makes the tip of the fibril more rough and less prone to adhere to the subtract.

A way to overcome this obstacle would be to control the concentration of the nanoparticles during the fabrication of the structures, so that a superior concentration of the NPs would be in the base of the fibril, with the objective of making the tip less rough and more adhesive.

5.3.2.1. FLAT HOMOGENEOUS PILLARS

Two flat, homogeneous pillars with the same area as the contact area of the structures being evaluated were fabricated (Figure 5.19). To offer a point of comparison for the microstructures A and B, the adhesion test conditions applied to these structures were the same as those applied to the previous microstructures.

Figure 5.19 – Flat samples fabricated with the same contact area as the structures A and B.

The plot of the Figure 5.20 shows the curves obtain from the testing of these structures.

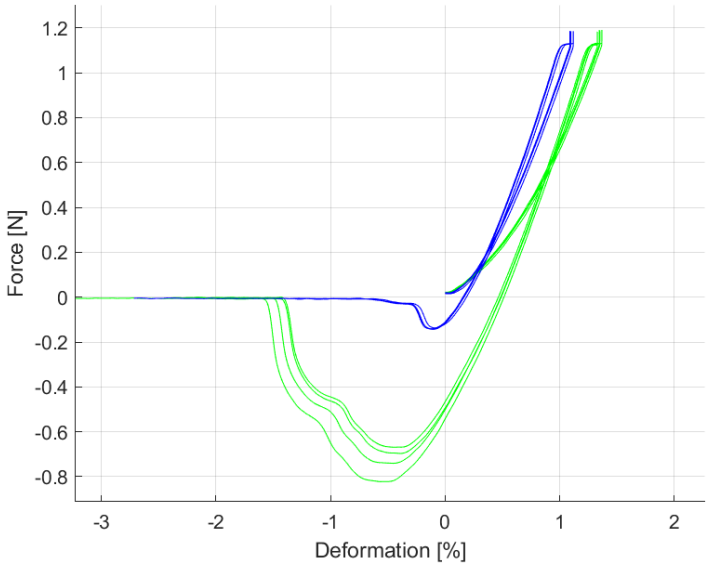

Figure 5.20 – Plot obtained after testing flat, homogeneous pillars. The blue curves correspond to the structure with a contact area of 98.5mm^2 (microstructure A) and the green to the contact area of 232.4mm^2 (microstructure B).

As it can be seen in Figures 5.20 and 5.21, the SHP with an apparent contact area of 232.4 mm^2 presents an enhanced performance above that anticipated due to the larger contact area.

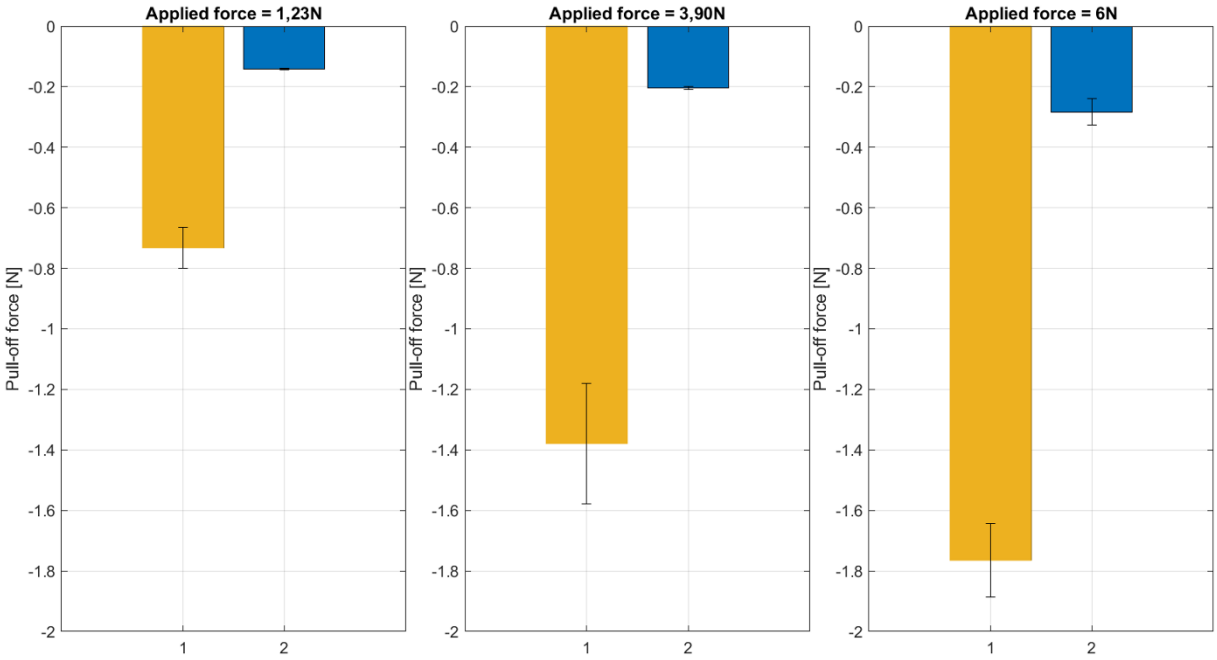

Figure 5.21 – Analysis of the data obtained from the Figure 5.19. The yellow columns represent the pillar with a contact area of 232.4 mm^2 and the blue columns represent the pillar with a contact area of 98.5 mm^2.

The data, as expected, shows that the pull-off force consistently increases with increasing applied force.

The geometry with the same area as microstructure A (98.5 mm^2) and microstructure A showed similar pull-off force results, leading to the conclusion that, in this specific case, splitting a large contact into thinner elements did not result in an increase in adhesion.

Analysing these surfaces under an optical microscope reveals that this phenomenon occurs because of the samples' surfaces. The structure's surface, with a diameter of 17,2 mm, appears significantly less rough than the other's (Figure 5.21). This occurrence can be attributed to an issue during the structure's fabrication.

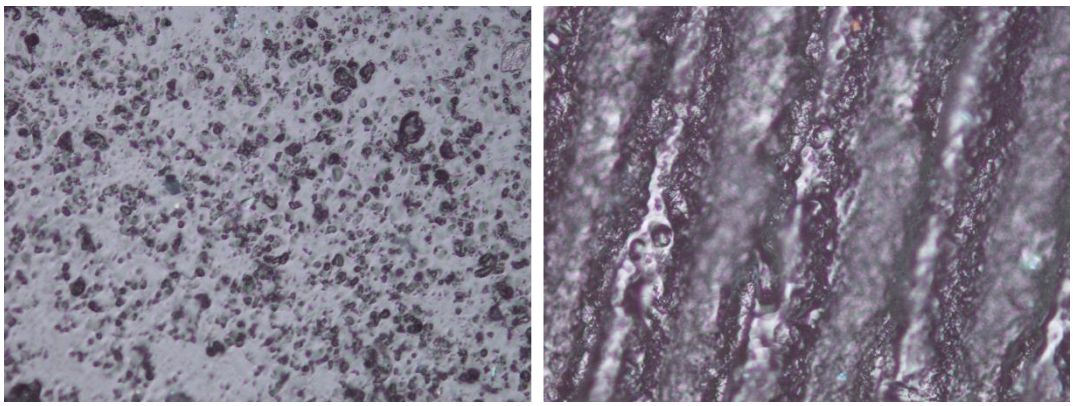

Figure 5.22 – Optical microscopy imagens. Left: SHP with a diameter of 17,2 mm; Right: SHP with a diameter of 11,2 mm.

6. CONCLUSIONS

Over the past several decades, our understanding about dry adhesion of micropatterned polymeric surfaces has matured. Instead of just surface energy and chemistry, mechanical factors play a major role at the adhesion performance. As a result, the development of high-performance micropatterned adhesives depends critically on the design of the contact geometry and the material characteristics.

In this work pillars with various diameters and aspect ratios were microstructured by using a *Sylgard 184* PDMS. To test the proposed pillars, it was performed adhesion experiments by using a flat compression plate with various preloads.

The main results obtain from this work can be summarized as follows:

- It was found that the silanization is a crucial process in negative molding. Without this process in the negative mold, the PDMS will bond with the negative mold material, Ecoflex 00-30.
- Reproducible patterned Sylgard 184 PDMS surfaces with a wide range of tip forms are possible to be made using a double casting molding technique and 3d Printing, paying special attention to the silanization method and the demolding.
- The adhesion characteristics of patterned surfaces are significantly influenced by the contact geometry and roughness.
- During the tests to the single pillars with different aspect ratios, the effect of this factor did not influence the adhesion.
- The adhesion shows to be dependent on the applied load. It also seems to present a critical load point beyond which it stabilizes, that is, with the increase of the applied force, the pull-off force increases up to a certain value.
- Comparing the two tested microstructures the highest pull-off forces were obtain for the array of pillars with the smaller radius.
- The flat homogenous pillars that have the same contact area as the microstructures tested showed better adhesion results.
- The PDMS structures surpassed the adhesion of the MRE structures by a wide margin. Because the microparticles increase the surface's roughness, this finding also demonstrates the influence of that characteristic. Developing these MRE

pillars without particles in the surface or on the cap could be a solution to prevent nano or microparticles from affecting the surface roughness.

In terms of future perspectives, design parameters such as the shape or design of the individual features themselves can be adjusted for further enhancement of the adhesive strength. For instance, varying the stalk length or diameter of the mushroom shape are just some of the possibilities that can be explored. Another future perspective is the development of MRE mushroom-shaped microstructures with different amounts of CIP in the cap zones than in the stalk/pillar zones, with the goal of reducing surface roughness.

To supplement the experiments on adhesion characterization, shear (or friction) adhesion tests (as suggested in Figure 2.17) could, potentially, be performed utilizing a tribometer (ultimately evaluating static friction).

REFERENCES

Aksak, B., Hui, C.-Y., & Sitti, M. (2011). The effect of aspect ratio on adhesion and stiffness for soft elastic fibres. *Journal of The Royal Society Interface*, *8*(61), 1166–1175. https://doi.org/10.1098/rsif.2010.0582

Arzt, E., Gorb, S., & Spolenak, R. (2003). From micro to nano contacts in biological attachment devices. *Proceedings of the National Academy of Sciences*, *100*(19), 10603–10606. https://doi.org/10.1073/pnas.1534701100

Arzt, E., Quan, H., McMeeking, R. M., & Hensel, R. (2021). Functional surface microstructures inspired by nature – From adhesion and wetting principles to sustainable new devices. *Progress in Materials Science*, *119*, 100778. https://doi.org/10.1016/j.pmatsci.2021.100778

Autumn, K. (2007). Gecko Adhesion: Structure, Function, and Applications. *MRS Bulletin*, *32*(6), 473–478. https://doi.org/10.1557/mrs2007.80

Autumn, K., Sitti, M., Liang, Y. A., Peattie, A. M., Hansen, W. R., Sponberg, S., Kenny, T. W., Fearing, R., Israelachvili, J. N., & Full, R. J. (2002). Evidence for van der Waals adhesion in gecko setae. *Proceedings of the National Academy of Sciences*, *99*(19), 12252–12256. https://doi.org/10.1073/pnas.192252799

Balijepalli, R. G., Begley, M. R., Fleck, N. A., McMeeking, R. M., & Arzt, E. (2016). Numerical simulation of the edge stress singularity and the adhesion strength for compliant mushroom fibrils adhered to rigid substrates. *International Journal of Solids and Structures*, *85–86*, 160–171. https://doi.org/10.1016/j.ijsolstr.2016.02.018

Balijepalli, R. G., Fischer, S. C. L., Hensel, R., McMeeking, R. M., & Arzt, E. (2017). Numerical study of adhesion enhancement by composite fibrils with soft tip layers. *Journal of the Mechanics and Physics of Solids*, *99*, 357–378. https://doi.org/10.1016/j.jmps.2016.11.017

Bastola, A. K., & Hossain, M. (2020). A review on magneto-mechanical characterizations of magnetorheological elastomers. *Composites Part B: Engineering*, *200*, 108348. https://doi.org/10.1016/j.compositesb.2020.108348

Becker, H., & Heim, U. (2000). Hot embossing as a method for the fabrication of polymer high aspect ratio structures. *Sensors and Actuators A: Physical*, *83*(1–3), 130–135. https://doi.org/10.1016/S0924-4247(00)00296-X

Betancourt, T., & Brannon-Peppas, L. (2006). Micro- and nanofabrication methods in nanotechnological medical and pharmaceutical devices. *International Journal of Nanomedicine*, *1*(4), 483–495. https://doi.org/10.2147/nano.2006.1.4.483

Borin, D., & Stepanov, G. (2022). Magneto-mechanical properties of elastic hybrid composites. *Physical Sciences Reviews*, *7*(10), 1119–1140. https://doi.org/10.1515/psr-2019-0126

Chai, Z., Liu, M., Chen, L., Peng, Z., & Chen, S. (2019). Controllable directional deformation of micro-pillars actuated by a magnetic field. *Soft Matter*, *15*(43), 8879–8885. https://doi.org/10.1039/C9SM01672D

Chan, E. P., Greiner, C., Arzt, E., & Crosby, A. J. (2007). Designing Model Systems for Enhanced Adhesion. *MRS Bulletin*, *32*(6), 496–503. https://doi.org/10.1557/mrs2007.84

Chou, S. Y., Krauss, P. R., & Renstrom, P. J. (1995). Imprint of sub-25 nm vias and trenches in polymers. *Applied Physics Letters*, *67*(21), 3114–3116. https://doi.org/10.1063/1.114851

del Campo, A., & Arzt, E. (2007). Design Parameters and Current Fabrication Approaches for Developing Bioinspired Dry Adhesives. *Macromolecular Bioscience*, *7*(2), 118–127. https://doi.org/10.1002/mabi.200600214

del Campo, A., Greiner, C., & Arzt, E. (2007). Contact Shape Controls Adhesion of Bioinspired Fibrillar Surfaces. *Langmuir*, *23*(20), 10235–10243. https://doi.org/10.1021/la7010502

Del Campo, A., Greiner, C., Álvarez, I., & Arzt, E. (2007). Patterned Surfaces with Pillars with Controlled 3D Tip Geometry Mimicking Bioattachment Devices. *Advanced Materials*, *19*(15), 1973–1977. https://doi.org/10.1002/adma.200602476

del Campo, A., Greiner, C., Álvarez, I., & Arzt, E. (2007). Patterned Surfaces with Pillars with Controlled 3D Tip Geometry Mimicking Bioattachment Devices. *Advanced Materials*, *19*(15), 1973–1977. https://doi.org/10.1002/adma.200602476

Dow Corning 184 Sylgard Silicone Elastomer. (n.d.). Https://Krayden.Com/Dow-Corning-184-Sylgard-Silicone-Elastomer-Kit/#:~:Text=The%20Dow%20Corning%20184%20Sylgard,Which%20is%20recommended%20for%20usage.

Drotlef, D.-M., Blümler, P., & del Campo, A. (2014). Magnetically Actuated Patterns for Bioinspired Reversible Adhesion (Dry and Wet). *Advanced Materials*, *26*(5), 775–779. https://doi.org/10.1002/adma.201303087

Ecoflex™ 00-30. (2022, April 14). Https://Www.Smooth-on.Com/Products/Ecoflex-00-30/.

Ecoflex™ Series. (n.d.). In *https://www.smooth-on.com/tb/files/ECOFLEX_SERIES_TB.pdf*.

Ellis, E. (2016, September 29). NASA's Gecko-Inspired Robots Can Climb Pretty Much Anything. *Https://Www.Wired.Com/2016/09/Nasas-Gecko-Inspired-Robots-Can-Climb-Pretty-Much-Anything/*.

Emil. (2021, June 15). *Column Buckling and why it's Important to Know About*. Https://Tribby3d.Com/Blog/Column-Buckling/.

Glassmaker, N. J., Jagota, A., & Hui, C.-Y. (2005). Adhesion enhancement in a biomimetic fibrillar interface. *Acta Biomaterialia*, *1*(4), 367–375. https://doi.org/10.1016/j.actbio.2005.02.005

Gorb, S., Varenberg, M., Peressadko, A., & Tuma, J. (2007). Biomimetic mushroom-shaped fibrillar adhesive microstructure. *Journal of The Royal Society Interface*, *4*(13), 271–275. https://doi.org/10.1098/rsif.2006.0164

Greiner, C., Arzt, E., & del Campo, A. (2009). Hierarchical Gecko-Like Adhesives. *Advanced Materials*, *21*(4), 479–482. https://doi.org/10.1002/adma.200801548

Greiner, C., del Campo, A., & Arzt, E. (2007). Adhesion of Bioinspired Micropatterned Surfaces: Effects of Pillar Radius, Aspect Ratio, and Preload. *Langmuir*, *23*(7), 3495–3502. https://doi.org/10.1021/la0633987

Greiner, C., Spolenak, R., & Arzt, E. (2009). Adhesion design maps for fibrillar adhesives: The effect of shape. *Acta Biomaterialia*, *5*(2), 597–606. https://doi.org/10.1016/j.actbio.2008.09.006

He, Q., Yu, M., Li, Y., Chen, X., Zhang, H., Gong, L., & Dai, Z. (2014). Adhesion characteristics of a novel synthetic polydimethylsiloxane for bionic adhesive pads. *Journal of Bionic Engineering*, *11*(3), 371–377. https://doi.org/10.1016/S1672-6529(14)60050-0

Heepe, L., & Gorb, S. N. (2014). Biologically Inspired Mushroom-Shaped Adhesive Microstructures. *Annual Review of Materials Research*, *44*(1), 173–203. https://doi.org/10.1146/annurev-matsci-062910-100458

Hensel, R., Moh, K., & Arzt, E. (2018). Engineering Micropatterned Dry Adhesives: From Contact Theory to Handling Applications. *Advanced Functional Materials*, *28*(28). https://doi.org/10.1002/adfm.201800865

IDP-3 Dry Scroll Vacuum Pump. (n.d.). In *https://www.agilent.com/*.

Jeong, H. E., Lee, J.-K., Kim, H. N., Moon, S. H., & Suh, K. Y. (2009). A nontransferring dry adhesive with hierarchical polymer nanohairs. *Proceedings of the National Academy of Sciences*, *106*(14), 5639–5644. https://doi.org/10.1073/pnas.0900323106

Johnston, I. D., McCluskey, D. K., Tan, C. K. L., & Tracey, M. C. (2014). Mechanical characterization of bulk Sylgard 184 for microfluidics and microengineering. *Journal of Micromechanics and Microengineering*, *24*(3), 035017. https://doi.org/10.1088/0960-1317/24/3/035017

Kamperman, M., Kroner, E., del Campo, A., McMeeking, R. M., & Arzt, E. (2010a). Functional adhesive surfaces with “Gecko” effect: The concept of contact splitting. In *Advanced Engineering Materials* (Vol. 12, Issue 5, pp. 335–348). https://doi.org/10.1002/adem.201000104

Kamperman, M., Kroner, E., del Campo, A., McMeeking, R. M., & Arzt, E. (2010b). Functional Adhesive Surfaces with “Gecko” Effect: The Concept of Contact Splitting. *Advanced Engineering Materials*, *12*(5), 335–348. https://doi.org/10.1002/adem.201000104

Kehagias, N., Francone, A., Guttmann, M., Winkler, F., Fernández, A., & Sotomayor Torres, C. M. (2018). Fabrication and replication of re-entrant structures by nanoimprint lithography methods. *Journal of Vacuum Science & Technology B*, *36*(6), 06JF01. https://doi.org/10.1116/1.5048241

Khaderi, S. N., Fleck, N. A., Arzt, E., & McMeeking, R. M. (2015). Detachment of an adhered micropillar from a dissimilar substrate. *Journal of the Mechanics and Physics of Solids*, *75*, 159–183. https://doi.org/10.1016/j.jmps.2014.11.004

Kim, D. S., Lee, H. S., Lee, J., Kim, S., Lee, K.-H., Moon, W., & Kwon, T. H. (2007). Replication of high-aspect-ratio nanopillar array for biomimetic gecko foot-hair prototype by UV nano embossing with anodic aluminum oxide mold. *Microsystem Technologies*, *13*(5–6), 601–606. https://doi.org/10.1007/s00542-006-0220-1

Kim, J. U., Lee, S., & Kim, T. (2016). Recent Advances in Unconventional Lithography for Challenging 3D Hierarchical Structures and Their Applications. *Journal of Nanomaterials*, *2016*, 1–17. https://doi.org/10.1155/2016/7602395

Kim, M., Moon, B.-U., & Hidrovo, C. H. (2013). Enhancement of the thermo-mechanical properties of PDMS molds for the hot embossing of PMMA microfluidic devices. *Journal of Micromechanics and Microengineering*, *23*(9), 095024. https://doi.org/10.1088/0960-1317/23/9/095024

Kim, T., Park, J., Sohn, J., Cho, D., & Jeon, S. (2016). Bioinspired, Highly Stretchable, and Conductive Dry Adhesives Based on 1D–2D Hybrid Carbon Nanocomposites for All-in-One ECG Electrodes. *ACS Nano*, *10*(4), 4770–4778. https://doi.org/10.1021/acsnano.6b01355

Lee, C., Kim, S. M., Kim, Y. J., Choi, Y. W., Suh, K.-Y., Pang, C., & Choi, M. (2015). Robust Microzip Fastener: Repeatable Interlocking Using Polymeric Rectangular Parallelepiped Arrays. *ACS Applied Materials & Interfaces*, *7*(4), 2561–2568. https://doi.org/10.1021/am507559d

Moon, M.-W., Cha, T.-G., Lee, K.-R., Vaziri, A., & Kim, H.-Y. (2010). Tilted Janus polymer pillars. *Soft Matter*, *6*(16), 3924. https://doi.org/10.1039/c0sm00126k

Murphy, M. P., Aksak, B., & Sitti, M. (2008). Gecko-Inspired Directional and Controllable Adhesion. *Small*, *5*(2), 170–175. https://doi.org/10.1002/smll.200801161

OnRobot. (n.d.).

Paretkar, D., Kamperman, M., Schneider, A. S., Martina, D., Creton, C., & Arzt, E. (2011). Bioinspired pressure actuated adhesive system. *Materials Science and Engineering: C*, *31*(6), 1152–1159. https://doi.org/10.1016/j.msec.2010.10.004

Parness, A., Abcouwer, N., Fuller, C., Wiltsie, N., Nash, J., & Kennedy, B. (2017). LEMUR 3: A limbed climbing robot for extreme terrain mobility in space. *2017 IEEE International Conference on Robotics and Automation (ICRA)*, 5467–5473. https://doi.org/10.1109/ICRA.2017.7989643

Peak. (2022, September 13). *What is High Speed Machining?* Https://Www.Peakedm.Com/WhatIsHighSpeedMachining.Html.

Pereira, C. (2022). *Development of an Optimal Magneto-Rheological Elastomer for Application on a Controllable Bioinspired Adhesive Mechanism for the Gripping System in Pick-n-Place Task*. University of Minho.

PLASMA PROCESS GASES. (n.d.). Harrickplasma.Com.

Qu, L., Dai, L., Stone, M., Xia, Z., & Wang, Z. L. (2008). Carbon Nanotube Arrays with Strong Shear Binding-On and Easy Normal Lifting-Off. *Science*, *322*(5899), 238–242. https://doi.org/10.1126/science.1159503

Sameoto, D., & Menon, C. (2010). Recent advances in the fabrication and adhesion testing of biomimetic dry adhesives. *Smart Materials and Structures*, *19*(10), 103001. https://doi.org/10.1088/0964-1726/19/10/103001

Sharma, P., Saggiomo, V., van der Doef, V., Kamperman, M., & A. Dijksman, J. (2021a). Hooked on mushrooms: Preparation and mechanics of a bioinspired soft probabilistic fastener. *Biointerphases*, *16*(1), 011002. https://doi.org/10.1116/6.0000634

Sharma, P., Saggiomo, V., van der Doef, V., Kamperman, M., & A. Dijksman, J. (2021b). Hooked on mushrooms: Preparation and mechanics of a bioinspired soft probabilistic fastener. *Biointerphases*, *16*(1), 011002. https://doi.org/10.1116/6.0000634

Shinohara, H., Goto, H., Kasahara, T., & Mizuno, J. (2013). Fabrication of a Polymer High-Aspect-Ratio Pillar Array Using UV Imprinting. *Micromachines*, *4*(2), 157–167. https://doi.org/10.3390/mi4020157

Sigma-Aldrich. (2022, May 4). Https://Www.Sigmaaldrich.Com/PT/En/Product/Aldrich/448931.

SLA 3D Printing. (n.d.). *Https://Www.Hubs.Com/Knowledge-Base/Sla-3d-Printing-Materials-Compared/*.

Spuskanyuk, A. V., McMeeking, R. M., Deshpande, V. S., & Arzt, E. (2008). The effect of shape on the adhesion of fibrillar surfaces. *Acta Biomaterialia*, *4*(6), 1669–1676. https://doi.org/10.1016/j.actbio.2008.05.026

Thackeray, K. (2022, April 11). *The Definitive Guide to ASTM D412 Tensile Testing of Elastomers*. Https://Www.Instron.Com/En-in/Testing-Solutions/Astm-Standards/Astm-D412.

Tian, T. F., Zhang, X. Z., Li, W. H., Alici, G., & Ding, J. (2013a). Study of PDMS based magnetorheological elastomers. *Journal of Physics: Conference Series*, *412*(1). https://doi.org/10.1088/1742-6596/412/1/012038

Tian, T. F., Zhang, X. Z., Li, W. H., Alici, G., & Ding, J. (2013b). Study of PDMS based magnetorheological elastomers. *Journal of Physics: Conference Series*, *412*, 012038. https://doi.org/10.1088/1742-6596/412/1/012038

Vaicekauskaite, J., Mazurek, P., Vudayagiri, S., & Skov, A. L. (2020). Mapping the mechanical and electrical properties of commercial silicone elastomer formulations for stretchable transducers. *Journal of Materials Chemistry C*, *8*(4), 1273–1279. https://doi.org/10.1039/C9TC05072H

Vieu, C., Carcenac, F., Pépin, A., Chen, Y., Mejias, M., Lebib, A., Manin-Ferlazzo, L., Couraud, L., & Launois, H. (2000). Electron beam lithography: resolution limits and applications. *Applied Surface Science*, *164*(1–4), 111–117. https://doi.org/10.1016/S0169-4332(00)00352-4

Wang, L., Ha, K.-H., Rodin, G. J., Liechti, K. M., & Lu, N. (2020). Mechanics of Crater-Enabled Soft Dry Adhesives: A Review. *Frontiers in Mechanical Engineering*, *6*. https://doi.org/10.3389/fmech.2020.601510

Wang, L., Yang, X., Wang, Q., Yang, Z., Duan, H., & Lu, B. (2017). Manufacturing of mushroom-shaped structures and its hydrophobic robustness analysis based on energy minimization approach. *AIP Advances*, *7*(7), 075110. https://doi.org/10.1063/1.4995419

Wang, Y., Hu, H., Shao, J., & Ding, Y. (2014). Fabrication of Well-Defined Mushroom-Shaped Structures for Biomimetic Dry Adhesive by Conventional Photolithography and Molding. *ACS Applied Materials & Interfaces*, *6*(4), 2213–2218. https://doi.org/10.1021/am4052393

Wang, Z. (2018). Slanted Functional Gradient Micropillars for Optimal Bioinspired Dry Adhesion. *ACS Nano*, *12*(2), 1273–1284. https://doi.org/10.1021/acsnano.7b07493

Wang, Z., Volinsky, A. A., & Gallant, N. D. (2014). Crosslinking effect on polydimethylsiloxane elastic modulus measured by custom-built compression instrument. *Journal of Applied Polymer Science*, *131*(22), n/a-n/a. https://doi.org/10.1002/app.41050

Zhao, R., Kim, Y., Chester, S. A., Sharma, P., & Zhao, X. (2019). Mechanics of hard-magnetic soft materials. *Journal of the Mechanics and Physics of Solids*, *124*, 244–263. https://doi.org/10.1016/j.jmps.2018.10.008

ANNEX A: DMA EXPERIMENTS

Some tests were also performed on a pillar with 1 mm radius and 2 mm height on a Dynamic mechanical analysis (DMA) machine.

In the graphs the sudden variation of the sample size is the moment of take-off.

First a compressive force of 0.005 N/min to 0.020 N was applied and then a force of -0.005 N/min to -0.100 N (Figure A.1).

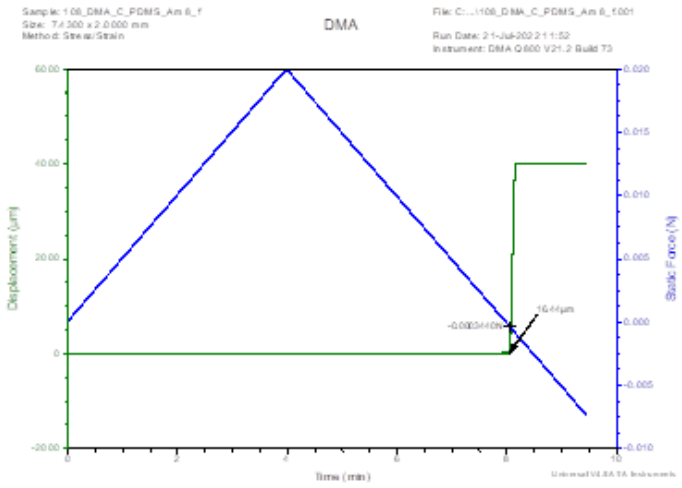

Figure A.1 – Plot obtained from the test performed on a DMA.

A test was also performed where a compressive force of 0.005 N/min to 0.010 N and subsequently a force of -0.005 N/min to -0.100 N was applied (Figure A.2).

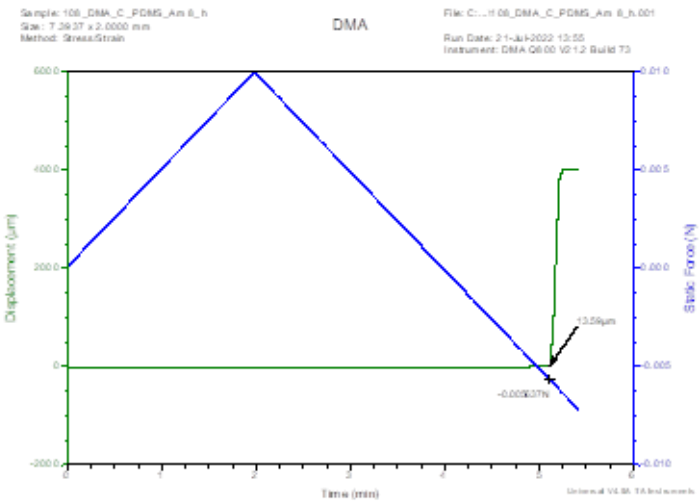

Figure A.2 – Plot obtained from the test performed on a DMA.